

AD-A090 137

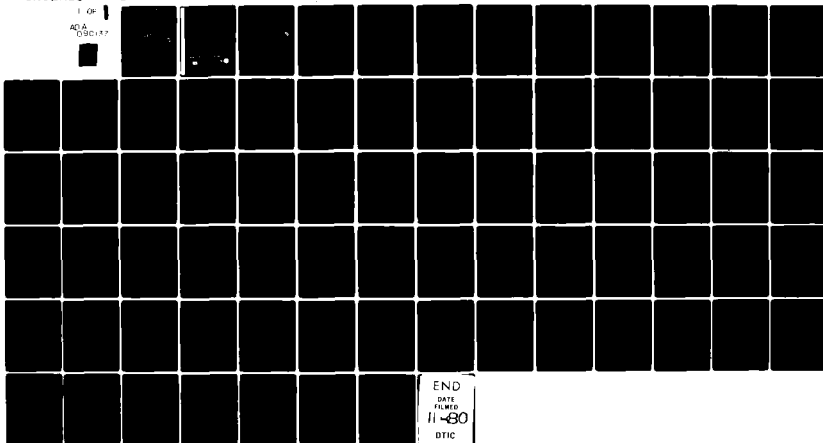
GEORGIA INST OF TECH ATLANTA ELECTROMAGNETIC EFFECTI--ETC F/G 20/14  
NEAR-FIELD THEORY AND TECHNIQUES FOR WIDEBAND RADIATING SYSTEMS--ETC(U)  
SEP 80 B J COWN, C E RYAN DAA629-78-C-0029

UNCLASSIFIED

ARO-15646.4-EL

NL

1 OF 1  
ADA  
090137



END  
DATE  
FILMED  
11-80  
DTIC

(12)

## REPORT DOCUMENTATION PAGE

READ INSTRUCTIONS  
BEFORE COMPLETING FORM

1. REPORT NUMBER 15646.4-EL	2. GOVT ACCESSION NO. AD-A090137	3. RECIPIENT'S CATALOG NUMBER
4. TITLE (and Subtitle) Near-Field Theory and Techniques for Wideband Radiating Systems at In-Band and Out-of-Band Frequencies,		5. TYPE OF REPORT & PERIOD COVERED Interim Technical: 1 Feb 79 - Mar 80.
7. AUTHOR(s) B. J. Cown C. E. Ryan, Jr.		6. PERFORMING ORG. REPORT NUMBER
9. PERFORMING ORGANIZATION NAME AND ADDRESS Georgia Institute of Technology Atlanta, GA 30332		8. CONTRACT OR GRANT NUMBER(s) DAAG29-78-C-0029
11. CONTROLLING OFFICE NAME AND ADDRESS U. S. Army Research Office Post Office Box 12211 Research Triangle Park, NC 27709		10. PROGRAM ELEMENT, PROJECT, TASK AREA & WORK UNIT NUMBERS
14. MONITORING AGENCY NAME & ADDRESS (if different from Controlling Office)		12. REPORT DATE Sep 80
LEVEL		13. NUMBER OF PAGES 65
16. DISTRIBUTION STATEMENT (of this Report) Approved for public release; distribution unlimited.		15. SECURITY CLASS. (of this report) Unclassified
17. DISTRIBUTION STATEMENT (of the abstract entered in Block 20, if different from Report) NA		15a. DECLASSIFICATION/DOWNGRADING SCHEDULE
18. SUPPLEMENTARY NOTES The view, opinions, and/or findings contained in this report are those of the author(s) and should not be construed as an official Department of the Army position, policy, or decision, unless so designated by other documentation.		
19. KEY WORDS (Continue on reverse side if necessary and identify by block number) antennas electromagnetic radiation numerical analysis CW antennas pulsed antennas		
20. ABSTRACT (Continue on reverse side if necessary and identify by block number) The basic theory and equations have been derived to describe the radiation characteristics of a wideband CW or pulsed antenna from measured near-field data and to describe the electromagnetic coupling characteristics of a near-field, cosited pair of wideband CW or pulsed antennas. The theory and equations are applicable for both in-band and out-of-band situations and for stochastic as well as deterministic processes. Numerical simulations have been conducted to validate the analytical results and gain insight into the general behavior of the radiation and coupling characteristics of CW antennas.		

DTIC  
SELECTED  
OCT 9 1980  
C

AD A090137

DDC FILE COPY

**INTERIM TECHNICAL REPORT NO. 2**  
**PROJECT A-2179**

**NEAR-FIELD THEORY AND TECHNIQUES FOR  
WIDEBAND RADIATING SYSTEMS AT IN-BAND  
AND OUT-OF-BAND FREQUENCIES**

**By**  
**B. J. Cown and C. E. Ryan, Jr.**

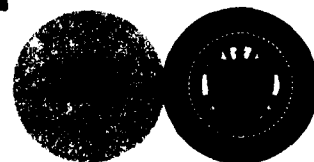
**CONTRACT NO. DAAG29-78-C-0029**

**FEBRUARY 1979 through MARCH 1980**

**Prepared for**  
**U. S. ARMY RESEARCH OFFICE**  
**P. O. BOX 12211**  
**RESEARCH TRIANGLE PARK**  
**NORTH CAROLINA 27709**

**GEORGIA INSTITUTE OF TECHNOLOGY**

**Engineering Experiment Station**  
**Atlanta, Georgia 30332**



**80 10 3 014**

INTERIM TECHNICAL REPORT NO. 2

PROJECT A-2179

NEAR-FIELD THEORY AND TECHNIQUES FOR WIDEBAND RADIATING SYSTEMS  
AT IN-BAND AND OUT-OF-BAND FREQUENCIES

By

B. J. Cown and C. E. Ryan, Jr.

Contract No. DAAG29-78-C-0029

February 1979 through March 1980

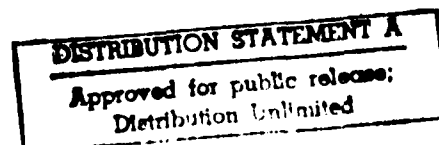


Prepared for

U.S. Army Research Office  
P.O. Box 12211  
Research Triangle Park, North Carolina 27709

Prepared by

Electromagnetic Effectiveness Division  
Electronics Technology Laboratory  
Engineering Experiment Station  
Georgia Institute of Technology  
Atlanta, Georgia 30332



## FOREWORD

The research on this program was performed by personnel of the Electromagnetic Effectiveness Division of the Electronics Technology Laboratory of the Engineering Experiment Station at the Georgia Institute of Technology, Atlanta, Georgia 30332. Dr. C. E. Ryan, Jr. served as the Project Director. This program is sponsored by the Army Research Office, P.O. Box 12211, Research Triangle Park, North Carolina 27709, and is designated by Georgia Tech as Project A-2179. This Interim Technical Report covers the period from February 1 1979 through March 1980. The report summarizes the key results obtained during this period and is provided for the purpose of disseminating technical information to interested parties. Technical discussions with and suggestions of Paul Majors of the U.S. Army Communications Research and Development Command, Ft. Monmouth, New Jersey 07703, are gratefully acknowledged.

Respectfully submitted,

*Barry J. Cown*

Barry J. Cown  
Associate Project Director

Approved:

*Charles E. Ryan Jr.*

Charles E. Ryan, Jr.  
Chief,  
EM Effectiveness Division

Accession For	
DTIS GRA&I	<input checked="checked" type="checkbox"/>
DTIC TAB	<input type="checkbox"/>
Unannounced	<input type="checkbox"/>
Justification	
By	
Distribution/	
Availability Codes	
Dist	Avail and/or
	Special
<b>A</b>	

## TABLE OF CONTENTS

<u>Section</u>	<u>Page</u>
I. INTRODUCTION. . . . .	1
II. NEAR-FIELD THEORY AND TECHNIQUES FOR WIDEBAND ANTENNA PATTERN CHARACTERIZATION. . . . .	5
A. Introduction . . . . .	5
B. Near-Field Covariance Study. . . . .	7
1. Analysis Wire Array. . . . .	9
2. Numerical Study of Wire Array. . . . .	14
III. NEAR-FIELD ANTENNA-ANTENNA COUPLING . . . . .	27
A. Introduction . . . . .	27
B. Spherical Wave Analysis. . . . .	27
C. Plane Wave Spectrum Analysis . . . . .	31
IV. SUMMARY . . . . .	63
V. REFERENCES. . . . .	65

## LIST OF FIGURES

<u>Figure</u>	<u>Page</u>
1. Sketch of an array of center-fed wire elements and near-field sample points. . . . .	10
2. Sketch showing array and near-field parameters for the numerical simulation, where $\lambda_0$ is the wavelength at the in-band frequency of 3.0 GHz . . . . .	16
3. Non-random near-field power distribution for the in-band frequency of 3.0 GHz for the in-band scan angle of 0 degrees. . . . .	17
4. Intrinsic (A) and total (B) near-field covariance function of the electric field at $y=0$ and the conjugate of the electric field at all other points on the near-field plane for the in-band frequency of 3 GHz for the in-band scan angle of 0 degrees. . . .	18
5. Intrinsic (A) and total (B) near-field covariance function of the electric field at $y=-20$ and the conjugate of the electric field at all other points on the near-field plane for the in-band frequency of 3 GHz for the in-band scan angle of 0 degrees. . . .	19
6. Analytical statistical average pattern for a nine-element dipole array of interacting (B) and non-interacting (A) elements for the in-band frequency of 3.0 GHz for the in-band scan angle of 0 degrees. . .	20
7. Non-random near-field power distribution for the out-of-band frequency of 9.0 GHz for the in-band scan angle of 0 degrees. . . . .	21
8. Intrinsic (A) and total (B) near-field covariance function of the electric field at $y=0$ and the conjugate of the electric field at all other points on the near-field plane for the out-of-band frequency of 9 GHz for the in-band scan angle of 0 degrees. . . .	22
9. Intrinsic (A) and total (B) near-field covariance function of the electric field at $y=-20$ and the conjugate of the electric field at all other points on the near-field plane for the out-of-band frequency of 9 GHz for the in-band scan angle of 0 degrees. . . .	23
10. Analytical statistical average pattern for a nine-element dipole array of interacting (B) and non-interacting (A) elements for the out-of-band frequency at 9.0 GHz for the in-band scan angle of 0 degrees. . .	24

# LIST OF FIGURES (Continued)

<u>Figure</u>		<u>Page</u>
11.	Sketch depicting two arbitrarily oriented near-field antennas and geometric parameters. . . . .	28
12.	Sketch depicting the azimuth rotation angle $\alpha$ and the elevation rotation angle $\xi$ . . . . .	29
13.	Sketch depicting the arrangement of two antennas appropriate for the PWS analysis of coupling . . . . .	32
14.	Sketch depicting the antenna aperture coordinates $Y_\ell, Z_k$ and the optical transform angle $\zeta_{\ell k}$ . . . . .	34
15.	Sketch of the near-field arrangement of Antenna A and Antenna B used in the numerical simulations. . . . .	37
16.	Far-field antenna pattern for Antenna A at the in-band frequency of 5.5 GHz for waveguide feed power flow entirely in the $TE_{10}$ mode . . . . .	39
17.	Far-field antenna pattern for Antenna B at the in-band frequency of 5.5 GHz for waveguide feed power flow entirely in the $TE_{10}$ mode . . . . .	40
18.	Far-field antenna pattern for Antenna A at the out-of-band frequency of 6.5 GHz for equal waveguide power flow in the $TE_{10}$ and $TE_{20}$ modes with relative phase angle of 0 degrees . . . . .	41
19.	Far-field antenna pattern for Antenna B at the out-of-band frequency of 6.5 GHz for equal waveguide power flow in the $TE_{10}$ and $TE_{20}$ modes with relative phase angle of 0 degrees . . . . .	42
20.	Far-field antenna pattern for Antenna A at the out-of-band frequency of 6.5 GHz for equal waveguide power flow in the $TE_{10}$ and $TE_{20}$ modes with relative phase angle of 35 degrees. . . . .	43
21.	Far-field antenna pattern for Antenna B at the out-of-band frequency of 6.5 GHz for equal waveguide power flow in the $TE_{10}$ and $TE_{20}$ modes with relative phase angle of -50 degrees . . . . .	44
22.	Mutual Gain versus rotation angle for both antennas operating in-band at 5.5 GHz for waveguide feed power flow entirely in the $TE_{10}$ mode for the longitudinal separation distance $X = 40$ feet and the transverse separation distance $Y = 0$ feet. . . . .	45



# LIST OF FIGURES (Continued)

<u>Figure</u>		<u>Page</u>
23.	Mutual Gain versus rotation angle for both antennas operating in-band at 5.5 GHz for waveguide feed power flow entirely in the $TE_{10}$ mode for the longitudinal separation distance $X = 40$ feet and the transverse separation distance $Y = 5$ feet. . . . .	46
24.	Mutual Gain versus rotation angle for both antennas operating in-band at 5.5 GHz for waveguide feed power flow entirely in the $TE_{10}$ mode for the longitudinal separation distance $X = 40$ feet and the transverse distance $Y = 10$ feet. . . . .	47
25.	Mutual Gain versus rotation angle for both antennas operating in-band at 5.5 GHz for waveguide feed power flow entirely in the $TE_{10}$ mode for the longitudinal separation distance $X = 20$ feet and the transverse separation distance $Y = 0$ feet. . . . .	48
26.	Mutual Gain versus rotation angle for both antennas operating in-band at 5.5 GHz for waveguide feed power flow entirely in the $TE_{10}$ mode for the longitudinal separation distance $X = 20$ feet and the transverse separation distance $Y = 5$ feet. . . . .	49
27.	Mutual Gain versus rotation angle for both antennas operating in-band at 5.5 GHz for waveguide feed power flow entirely in the $TE_{10}$ mode for the longitudinal separation distance $X = 20$ feet and the transverse separation distance $Y = 10$ feet . . . . .	50
28.	Mutual Gain versus rotation angle for both antennas operating in-band at 5.5 GHz for waveguide feed power flow entirely in the $TE_{10}$ mode for the longitudinal separation distance $X = 10$ feet and the transverse separation distance $Y = 0$ feet . . . . .	51
29.	Mutual Gain versus rotation angle for both antennas operating in-band at 5.5 GHz for waveguide feed power flow entirely in the $TE_{10}$ mode for the longitudinal separation distance $X = 10$ feet and the transverse separation distance $Y = 5$ feet. . . . .	52
30.	Mutual Gain versus rotation angle for both antennas operating out-of-band at 6.5 GHz for equal waveguide feed power flow in the $TE_{10}$ and $TE_{20}$ modes with relative phase angle of 0 degrees for the longitudinal separation distance $X = 40$ feet and the transverse separation distance $Y = 0$ feet . . . . .	53

# LIST OF FIGURES (Continued)

<u>Figure</u>		<u>Page</u>
31.	Mutual Gain versus rotation angle for both antennas operating out-of-band at 6.5 GHz for equal waveguide feed power flow in the $TE_{10}$ and $TE_{20}$ modes with relative phase angle of 0 degrees for the longitudinal separation distance $X = 40$ feet and the transverse separation distance $Y = 5$ feet . . . . .	54
32.	Mutual Gain versus rotation angle for both antennas operating out-of-band at 6.5 GHz for equal waveguide feed power flow in the $TE_{10}$ and $TE_{20}$ modes with relative phase angle of 0 degrees for the longitudinal separation distance $X = 40$ feet and the transverse separation distance $Y = 10$ feet. . . . .	55
33.	Mutual Gain versus rotation angle for both antennas operating out-of-band at 6.5 GHz for equal waveguide feed power flow in the $TE_{10}$ and $TE_{20}$ modes with relative phase angle of 0 degrees for the longitudinal separation distance $X = 20$ feet and the transverse separation distance $Y = 0$ feet . . . . .	56
34.	Mutual Gain versus rotation angle for both antennas operating out-of-band at 6.5 GHz for equal waveguide feed power flow in the $TE_{10}$ and $TE_{20}$ modes with relative phase angle of 0 degrees for the longitudinal separation distance $X = 20$ feet and the transverse separation distance $Y = 5$ feet . . . . .	57
35.	Mutual Gain versus rotation angle for both antennas operating out-of-band at 6.5 GHz for equal waveguide feed power flow in the $TE_{10}$ and $TE_{20}$ modes with relative phase angle of 0 degrees for the longitudinal separation distance $X = 20$ feet and the transverse separation distance $Y = 10$ feet. . . . .	58
36.	Mutual Gain versus rotation angle for both antennas operating out-of-band at 6.5 GHz for equal waveguide feed power flow in the $TE_{10}$ and $TE_{20}$ modes with relative phase angle of 0 degrees for the longitudinal separation distance $X = 10$ feet and the transverse separation distance $Y = 0$ feet . . . . .	59
37.	Mutual Gain versus rotation angle for both antennas operating out-of-band at 6.5 GHz for equal waveguide feed power flow in the $TE_{10}$ and $TE_{20}$ modes with relative phase angle of 0 degrees for the longitudinal separation distance $X = 10$ feet and the transverse separation distance $Y = 5$ feet . . . . .	60

# LIST OF FIGURES (Co ntinued)

<u>Figure</u>		<u>Page</u>
38.	Mutual Gain versus rotation angle for both antennas operating out-of-band at 6.5 GHz forequal waveguide feed power flow in the $TE_{10}$ and $TE_{20}$ modes with relative phase of 35 degrees for Antenna A and -50 degrees for Antenna B for the longitudinal separation distance $X = 20$ feet and the transverse separation distance $Y = 5$ feet. . . . .	61

## SECTION I

### INTRODUCTION

The progress and results achieved to date on this basic research program are summarized herein. The purpose of the research program is to study the application of near-field techniques to characterize the radiation and coupling characteristics of wideband CW or pulsed radiators. Out-of-band as well as in-band situations are of interest and both situations are included in the study. Experience has shown that the radiation characteristics of out-of-band radiators may be very erratic and unpredictable. Consequently, statistical analysis techniques are needed for out-of-band characterization. However, statistical techniques and concepts can also be employed to provide succinct EMC descriptions of "deterministic" in-band wideband or pulsed radiators. Consequently, a considerable effort has been devoted to statistical characterization of wideband radiators.

The research program is divided into four major tasks. The four tasks are as follows.

Task 1. Provide a near-field methodology to characterize electromagnetic emitter radiation patterns at in-band and out-of-band frequencies for wide bandwidth radiators. The objective of this task is to develop the appropriate theory and equations based on statistical analysis techniques for efficient characterization of wideband radiators.

Task 2. Theoretically relate the radiation pattern characterization methodology to the data needs of electromagnetic spectrum usage optimization analysis. The objective of this task is to relate the near-field derived wideband antenna characterization to the performance of transmitting and receiving systems which co-exist in the same EM environment.

Task 3. Provide the methodology to assess the effects of system devices (i.e., higher-order mode generation) on the radiation pattern. The objective of this task is to determine a method whereby the pattern effects of higher-order modes which are generated by system devices at out-of-band frequencies can be assessed.

Task 4. Investigate the impact of site effects on the near-field antenna analysis technology. The objective of this task is to extend the existing monochromatic spectrum scattering matrix analysis to study antenna siting effects on the wideband and out-of-band performance of radiating systems.

The research efforts on the various tasks are being conducted in accordance with the amended program schedule presented on Page 3. Accordingly, the efforts thus far have been directed toward Task 1 and Task 2.

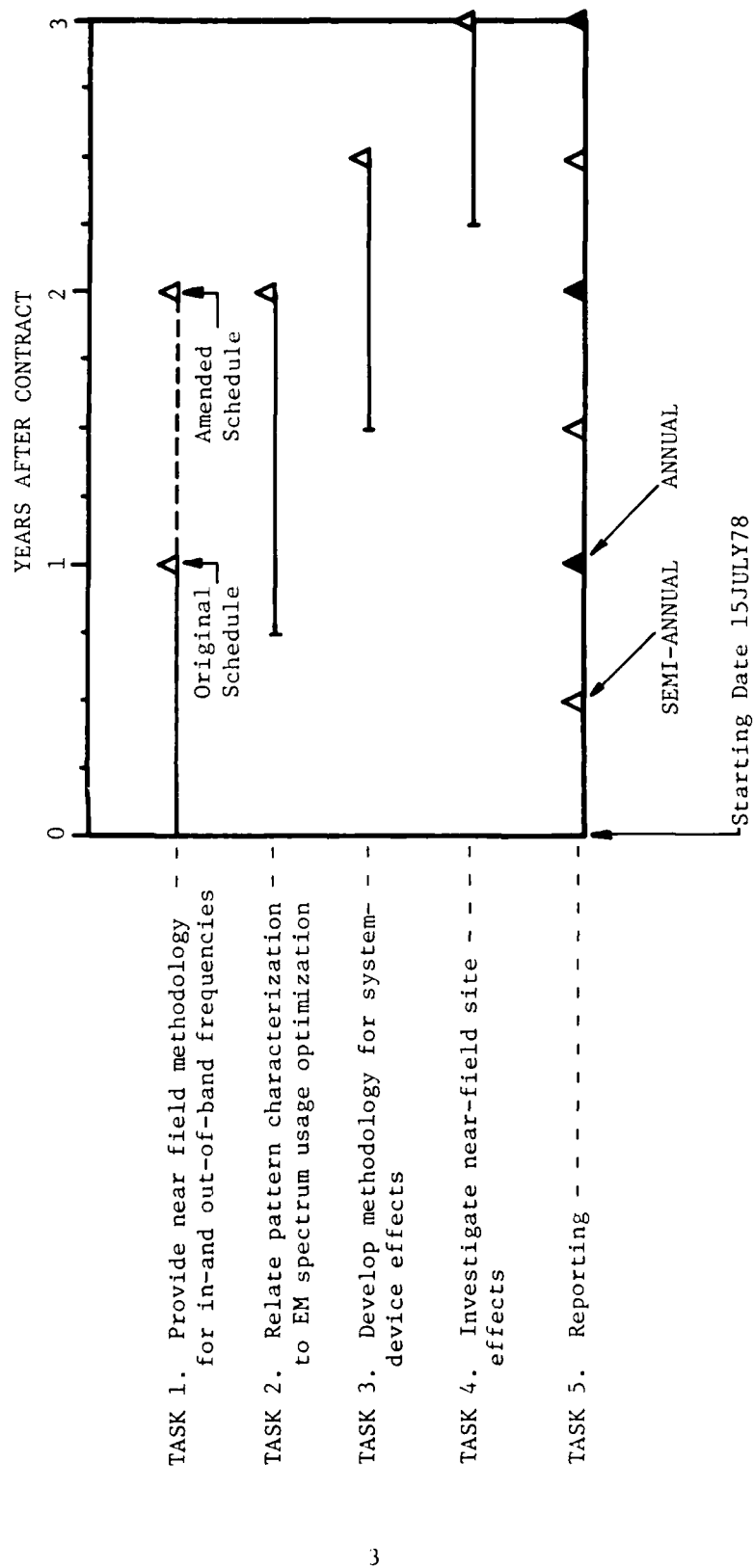
The approach taken to accomplish the objectives of Task 1 consists of research efforts on the following three subtasks.

- (a) Develop the theory for both in-band and out-of-band frequencies for deriving statistical average far-field patterns from wide-band or pulsed near-field measurements. This study will concentrate on methods to derive valid far-zone pattern statistics by either defining a minimum set of required near-field data or by developing optimum near-field data processing techniques such as averaging or time domain pulse synthesis.
- (b) Based upon the theoretical studies, methods of efficiently characterizing both wideband continuous-wave and pulsed radiators using near-field measurement techniques will be devised and studied. The basic limitations of these methods will be identified, and the expected accuracy of each of the techniques will be assessed.
- (c) Based upon the theoretical studies, a numerical simulation which will be applicable to various antenna types, such as reflector and phased-array antennas, will be developed to demonstrate that valid statistical far-field pattern distributions can be obtained from near-field measurements.

The objectives of Task 2 are being accomplished by research on the following three sub-tasks.

- (a) Develop the theory for analyzing the coupling between co-sited transmitting and receiving systems. This research will concentrate on the development of methods to characterize interference at both in-band and out-of-band frequencies which is due to both harmonic generation and wideband interference due to the wide frequency spectrum of a short pulse. It is anticipated that these techniques will be based upon the spectral scattering matrix theory.

# PROGRAM SCHEDULE Out-of-Band EMC Measurement Techniques



- (b) Develop the theory to efficiently describe the EM coupling mechanisms which can exist for combinations of wideband transmitting antennas, narrowband-harmonic transmitting antennas, and both wideband and narrowband-harmonic receiving antennas.
- (c) Based upon the theoretical studies, the minimum near-field derived data required for efficient EM spectrum usage optimization will be defined. This minimum defined data set will be employed in numerical simulations to demonstrate application to EM spectrum usage analysis.

Preliminary theoretical and numerical results are presented in Section II for Task 1 and Section III for Task 2. A synopsis of overall results and scheduled future efforts is presented in Section IV.

SECTION II  
NEAR-FIELD THEORY AND TECHNIQUES FOR  
WIDEBAND ANTENNA PATTERN CHARACTERIZATION

A. Introduction

The basic theory and equations for characterizing wideband in-band and out-of-band power patterns from measured near-field data have been derived. The theory and equations applicable to both wideband continuous wave (CW) and pulsed antennas have been presented and discussed in the Interim Technical Report No. 1 [ 1 ]. Deterministic as well as statistical analyses were conducted as appropriate to derive explicit equations for predicting and describing wideband antennas at both in-band and out-of-band frequencies. The analyses and numerical simulations presented in the previous report were conducted for a linear phased array antenna in order to gain insight into the basic physics of the wideband problem. However, the general results of the analysis are applicable to real-world antennas. The key results obtained via the analysis presented in the Report No. 1 and through subsequent analysis for the more realistic two-dimensional situation since the previous report was issued are summarized below:

- (1) The statistical average patterns and standard deviations at selected frequencies can provide a very succinct engineering description of the important EMC characteristics of wideband CW multimoding antennas. The statistical average patterns and standard deviations are a practical alternative to the comparatively more expensive and cumbersome Monte Carlo simulations.
- (2) The statistical average pattern for a given frequency may be computed from a knowledge of the following near-field statistical parameters:
  - (a) statistical average value of the electric field at all near-field measurement points,
  - (b) the standard deviation of the electric field at all measurement points, and
  - (c) the covariance functions for the electric fields at all different near-field measurement points.
- (3) The statistical average pattern versus time for a pulsed system depends on all of the above near-field statistical parameters



listed in Item 2, and the following far-field statistical parameters:

- (a) the statistical average value of the far-field electric field at all frequencies in the frequency band,
- (b) the standard deviation of the far-field electric field at all frequencies in the frequency band, and
- (c) the covariance functions of the electric fields at all different frequencies in the frequency band.

However, the far-field statistical parameters listed above can be computed from the near-field statistical parameters. Thus, pulsed antennas characterization does not require knowledge of any additional statistical near-field data.

These results imply that the fundamental technical requirement for employing near-field techniques to describe wideband CW or pulsed antenna radiation is that one be able to compute the statistical average far-field power pattern versus frequency from the measured near-field data. As stated in Item 2, this requires a knowledge of the average electric field and the standard deviation at each sample point and the covariance function at all different measurement points (cross-covariance). Only the cross-covariance function presents a significant measurement problem. The accuracy and feasibility of the near-field measurement technique for wideband out-of-band antennas hinge on whether the covariance functions can be suitably determined. Accordingly, considerable effort has been devoted to studying the covariance functions and their impact on accuracy, time and cost. The results of this effort are presented and discussed in subsection B. In particular, the theoretical and numerical analyses are presented for a linear array of wire elements. The theory and equations for a two dimensional array of wire elements involve no new concepts. Corresponding theoretical and numerical analyses of an array of multimoding out-of-band waveguide elements can be performed in the near future if deemed appropriate. This decision can best be made later after the question of whether the covariance functions can be efficiently recovered from the near-field data is resolved.

## B. Near-Field Covariance Study

The fact that the electric fields at different near-field sample points are correlated has an impact on the measurement time, accuracy and cost which can be appreciated by considering two different measurement schemes using a single probe to measure a wideband phased array antenna. The two measurement schemes will be denoted for convenience as Method I and Method II.

In Method I, data are recorded as the probe is moved over the measurement plane in a raster scan. The operating frequency and array scan condition are assumed to be constant while the probe scans the entire measurement plane. This takes about two hours of elapsed time. The probe is then returned to its starting point, and the array phase shifters are "cycled" and returned to the initial scan condition. Data are recorded at the same frequency as the probe again traverses the measurement plane. This sequence of events is repeated, say, 50 times for a given frequency and array scan condition. The total measurement time required to record data for 100 frequencies and 30 array scan conditions is about 300,000 hours. The measurement time is clearly excessive. Additionally, it is very unlikely that an out-of-band array antenna under test can be kept stable, i.e., no variation in modal content in any element, for the two-hours needed to record data for each selected out-of-band frequency and array scan condition. However, if the array element signals could be kept stable the near-field covariance functions could be computed directly from the measured data.

In Method II, the probe is held stationary at a preselected sample point while the signal source is scanned through the entire frequency spectrum of interest for a given array scan condition. The phase shifters are then cycled and returned to the selected scan condition. This procedure is repeated 50 times. A new scan condition is selected and the foregoing sequence of events is repeated. Finally, the entire sequence of events is repeated for all of the preselected sample measurement points on the near-field plane. Total measurement time for 100 frequencies and 30 array scan conditions is estimated to be about 120 hours. This measurement time is

reasonable for a thorough characterization of a randomly-excited, out-of-band, wide-band phased array antenna. The average value and standard deviation of the electric field at each near-field sample point can be computed directly from the recorded data for each frequency and scan condition. However, the covariance function for the electric fields at different near-field sample points can not be computed directly from the recorded data.

The question of whether the covariance functions can be recovered from the measured data through subsequent (software) processing based on statistical analysis equations is currently under investigation. Any conclusions this early in the investigations would be premature. However, it is anticipated that this question will be resolved in the next few months.

The covariance functions for the near-field electric field of a given array can be computed in a straightforward manner in terms of the covariance function for the electric fields on the array aperture. Of course, the aperture covariance function is not known in practice. If it were known, there would be no need for near-field measurements. However, an analysis of a specified array antenna can be used to study the general nature of the near-field covariance functions and their impact on the accuracy of the far-field average power pattern calculations. Furthermore, near-field covariance functions computed in this manner provide baseline data that can be used to check the validity and accuracy of near-field covariance functions obtained from analysis of simulated measured data obtained from a simulated Method II measurement. Accordingly, the near-field covariance functions for a linear array of wire dipoles have been studied analytically and numerically. A corresponding study for an array of multimoding waveguide elements would be beneficial but evidently could be accomplished only at the expense of amending the program schedule shown on page 3 and the scope of the remaining tasks. This is a matter for discussion among cognizant personnel at ARO, CORADCOM, and Georgia Tech in the near future.

### 1. Analysis of Wire Array

The linear array of vertically-oriented, center-fed wire elements shown in Figure 1 is analyzed in the following paragraphs. It is assumed in the analysis that each element is fed by a constant voltage source.

The electric field  $E_q$  at measurement point  $q$  on the line defined by  $Z=0$ ,  $X=X_0$  is  $Z$ -directed and is given as

$$E_q = \text{const.} \times \sum_{\ell} I_{\ell} \frac{\exp[-jk \sqrt{k_o^2 + (Y_q - Y_{\ell})^2}]}{\sqrt{k_o^2 + (Y_q - Y_{\ell})^2}} \quad (1)$$

where

$I_{\ell}$  = complex current at the current amplitude maximum on the  $\ell^{\text{th}}$  element,

$Y_q$  = the  $Y$  coordinate of the  $q^{\text{th}}$  measurement sample point,

$Y_{\ell}$  = the  $Y$  coordinate of the  $\ell^{\text{th}}$  element,

$k = 2\pi/\lambda$  where  $\lambda$  is the wavelength, and

$$\text{const.} = \frac{j\omega\mu}{4\pi} \int_{-h/2}^{+h/2} d(z') e^{-jk_z z'} dz'.$$

The integral appearing in the definition of const. is the same for each element at a given frequency and is just the Fourier Transform of the current distribution  $d(z')$  along the length of the element, where  $d(z')$  is normalized to have a maximum amplitude of 1.0. Const. will be suppressed in most of the remaining equations.

The statistical average far-field power density  $\langle P(\phi) \rangle$  at azimuth angle  $\phi$  can be computed as

$$\langle P(\phi) \rangle = \langle E^*(\phi) \rangle \langle E(\phi) \rangle + \sum_q \sum_q C_{q,q} \exp [(jk \sin \phi)(Y_q - Y_q)] \quad (2)$$

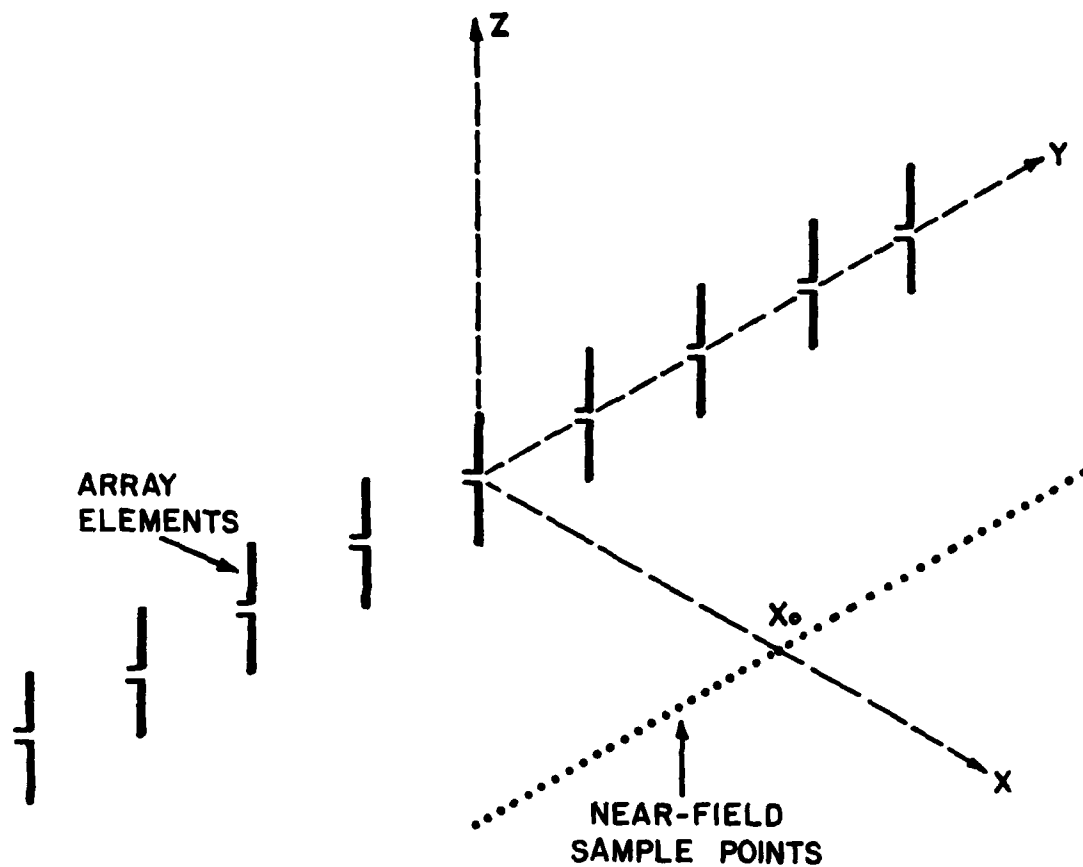


Figure 1. Sketch of an array of center-fed wire elements and near-field sample points.

where  $\langle E(\phi) \rangle$  is the Fourier Transform of the average near-field electric field and  $\langle E^*(\phi) \rangle$  is its complex conjugate.  $C_{q,q}$  is the near-field covariance function. The angular brackets denote statistical ensemble averages of the form

$$\langle W(\chi) \rangle = \int_{\xi_1} \dots \int_{\xi_n} W(\chi | \xi_1 \dots \xi_n) f(\xi_1 \dots \xi_n) d\xi_1 \dots d\xi_n \quad (3)$$

where

$\chi$  = non-random variables,  
 $\xi$  = random variables, and  
 $f(\xi)$  = joint probability density function for the random variables.

The near-field covariance function  $C_{q,q}$  is by definition

$$C_{q,q} = \langle E_q^*, E_q \rangle - \langle E_q^* \rangle \langle E_q \rangle \quad (4)$$

where the symbol  $*$  denotes complex conjugation. The near-field covariance function  $C_{q,q}$  obtained from Equations (1) and (4) is then explicitly computed as

$$C_{q,q} = \sum_{\ell'} \sum_{\ell} C_{\ell',\ell} G_{\ell',q}^* G_{\ell,q} \quad (5)$$

where

$C_{\ell',\ell}$  = the covariance function for the current on element  $\ell$  and the conjugate of the current on element  $\ell'$ , and

$$G_{\ell',q}^* G_{\ell,q} = \frac{\exp \left\{ jk_0 \left[ \sqrt{X_o^2 + (Y_{q'} - Y_{\ell'})^2} - \sqrt{X_o^2 + (Y_q - Y_{\ell})^2} \right] \right\}}{\sqrt{X_o^2 + (Y_{q'} - Y_{\ell'})^2} \sqrt{X_o^2 + (Y_q - Y_{\ell})^2}} \quad (6)$$

The current covariance function  $C_{\ell, \ell}$  is by definition

$$C_{\ell, \ell} = \langle I_{\ell}^*, I_{\ell} \rangle - \langle I_{\ell}^* \rangle \langle I_{\ell} \rangle . \quad (7)$$

Equations (5) and (7) express the fact that the near-field covariance function can be computed from the current covariance function.

The current covariance function  $C_{\ell, \ell}$  is a function of the mutual admittance matrix for the array and the statistical parameters of the input voltage sources. In particular, the current at the  $\ell^{\text{th}}$  element is computed as

$$I_{\ell} = \sum_{\kappa} \Gamma_{\ell \kappa} V_{\kappa} \quad (8)$$

where

$\Gamma_{\ell \kappa}$  = elements of the complex admittance matrix, and

$V_{\kappa}$  = complex voltage of the  $\kappa^{\text{th}}$  voltage source.

It follows then that  $C_{\ell, \ell}$  is computed as

$$C_{\ell, \ell} = \sum_{\kappa} \sum_{\kappa'} \Gamma_{\ell \kappa}^* \Gamma_{\ell \kappa'} C_{\kappa, \kappa'} \quad (9)$$

where  $C_{\kappa, \kappa'}$  is the voltage covariance function.

The current covariance function has zero magnitude in two different special cases. First, the current covariance function is zero when all of the voltage covariance functions are zero. This occurs when the voltages are deterministic (non-random). The currents are then perfectly correlated with correlation coefficient  $R_{\ell, \ell} = 1.0$  as can be discerned from the equation

$$R_{\ell, \ell} = \frac{C_{\ell, \ell}}{\xi_{\ell}^2} \quad , \quad (10)$$

where  $\xi_{\ell}$  = standard deviation of the complex current, by taking the limit as the numerator and denominator approach zero. Second, the current covariance function for  $\ell \neq \ell'$  is zero when, simultaneously, the voltages are uncorrelated and the mutual coupling between current elements is zero. In this case the voltage covariance  $C_{\kappa, \kappa} = \delta_{\kappa, \kappa} (\gamma_v^2)_{\kappa}$  and  $\Gamma_{\ell \kappa} = \delta_{\ell \kappa} \Gamma_{\ell}$ , i.e., the voltage covariance matrix and the mutual admittance matrix both contain non-zero matrix elements only along the diagonal. This second case, where  $C_{\ell, \ell} = 0$  for  $\ell \neq \ell'$ , corresponds to the situation where the currents on different elements are uncorrelated and hence  $C_{\ell, \ell} = \delta_{\ell, \ell} \xi_{\ell}^2$ .

It will be assumed in the rest of the analysis that the voltage sources are statistically independent and are therefore uncorrelated. The behavior of the near-field covariance function will be examined for the case involving isolated current elements ( $\Gamma_{\ell \kappa} = \delta_{\ell \kappa} \Gamma_{\ell}$ ) and the case involving mutual coupling among the current elements.

The near-field covariance function may be written as

$$C_{q, q} = \sum_{\ell} |\Gamma_{\ell \ell}|^2 (\gamma_v^2)_{\ell} G_{\ell q}^* G_{\ell q} + \sum_{\ell} \sum_{\ell'} \Gamma_{\ell' \kappa}^* \Gamma_{\ell \kappa} (\gamma_v^2)_{\kappa} (1 - \delta_{\ell' \kappa} \delta_{\ell \kappa}) G_{\ell', q}^* G_{\ell q} \quad (11)$$

for the realistic situation when the currents are coupled and as

$$C_{q, q} = \sum_{\ell} |\Gamma_{\ell \ell}|^2 (\gamma_v^2)_{\ell} G_{\ell q}^* G_{\ell q} \quad (12)$$

when the element currents are not coupled. Equation (12) is obtained



from Equation (11) by setting  $\Gamma_{\ell' \kappa}^* \Gamma_{\ell \kappa} = \delta_{\ell' \kappa} \delta_{\ell \kappa}$  so that the off-diagonal elements of the mutual admittance matrix are zero. Equation (12) shows that the near-field covariance function is non-zero even if the near-field electric field is produced by isolated, statistically independent currents. This covariance will be denoted for convenience as intrinsic covariance. It is always present in stochastic antenna problems. Equation (11) shows that the total near-field covariance function in the realistic situation involving coupled radiating elements consists of two components, namely the intrinsic covariance and a second component denoted herein as the interactive covariance. The interactive covariance is present only when the radiating elements "interact", i.e., are electromagnetically coupled. A third component of the near-field covariance function, denoted as the intra-element covariance, occurs for multimoding waveguide antennas due to correlation among the modes propagating within each separate waveguide element proper. This covariance contribution is absent for the wire array under consideration.

It should be noted that the near-field covariance function for the wire array given by Equations (11) and (12) are scan-invariant. This result follows from the fact that the mutual admittances are scan-invariant. Of course, the statistical average amplitudes and relative phases of the electric field at each sample point do change with scan angle. The near-field covariance functions for a multimoding out-of-band waveguide array may change with scan angle due to changes in average mode excitations with scan angle.

## 2. Numerical Study of Wire Array

Numerical simulations were conducted to study both the near-field and far-field radiation characteristics of a linear array of nine center-fed wire elements. The array elements have length  $\lambda_0/2$ , where  $\lambda_0$  is the free-space wavelength at the design in-band frequency of 3.0 GHz, and are spaced  $\lambda_0/2$  apart along the y axis. Each wire element is assumed to be fed by a constant amplitude voltage source, and each source is assumed to be matched to a 50-ohm line at both in-band and out-of-band frequencies.

The following data were computed for an array of coupled elements and an array of "isolated" elements for both the in-band frequency of 3.0 GHz and the out-of-band frequency of 9.0 GHz:

- (1) Non-random (deterministic) near-field power distributions and far-field power patterns,
- (2) Random (Monte Carlo) near-field power distributions and far-field power patterns,
- (3) Analytical statistical average near-field power distribution and analytical statistical average far-field power pattern,
- (4) Numerical average far-field pattern and its associated standard deviation based on 50 Monte Carlo random far-field patterns, and
- (5) Near-field covariance functions.

The data for Items (1) through (4) were computed for in-band scan-angles of zero degrees and 30 degrees. The near-field covariance functions for the wire array are scan-invariant and, hence, they were explicitly computed only for the broadside (zero-degree) scan condition.

The near-field covariance functions and their effects on the statistical average power patterns are the topics of paramount interest and only these data will be presented and discussed herein. A sketch of the simulated near-field measurement situation is shown in Figure 2. The near-field data were computed for 65 sample points centered on the near-field sample line. The near-field sample line was chosen to be  $8\lambda_0$  wide and is located  $2\lambda_0$  from the array.

The key results of the numerical studies can be summarized with the aid of the data plotted in the group of Figures 3 through 6 for the in-band frequency of 3.0 GHz and the group of Figures 7 through 10 for the out-of-band frequency of 9.0 GHz. The data are sequenced in the same order within each group. The first figure in each group is a plot of the near-field power distribution for deterministic (non-random) excitation of an array of coupled current elements for broadside scan. This plot is followed by plots of the scan-invariant, near-field statistical covariance functions and plots of the corresponding statistical average far-field power patterns for broadside scan. The statistical data in each figure are displayed for

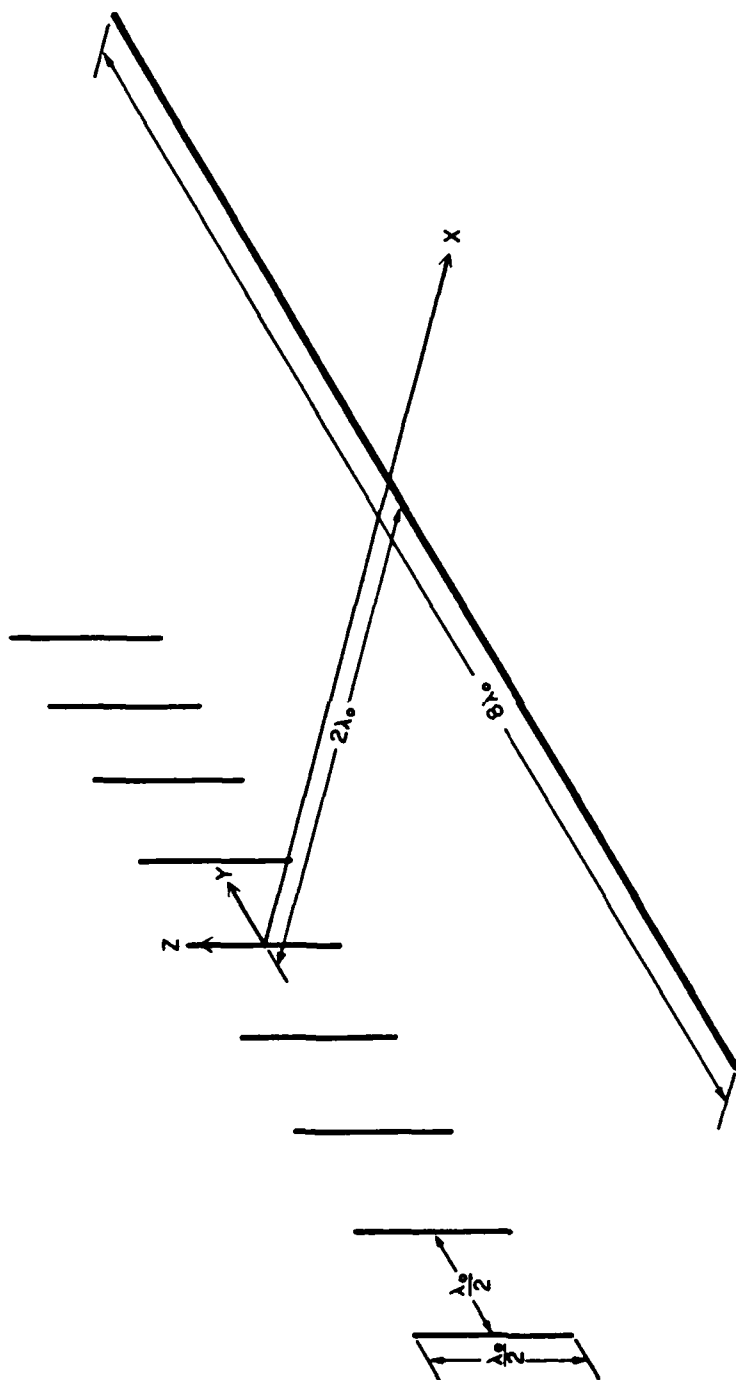


Figure 2. Sketch showing array and near-field parameters for the numerical simulation, where  $\lambda_0$  is the wavelength at the in-band frequency of 3.0 GHz.

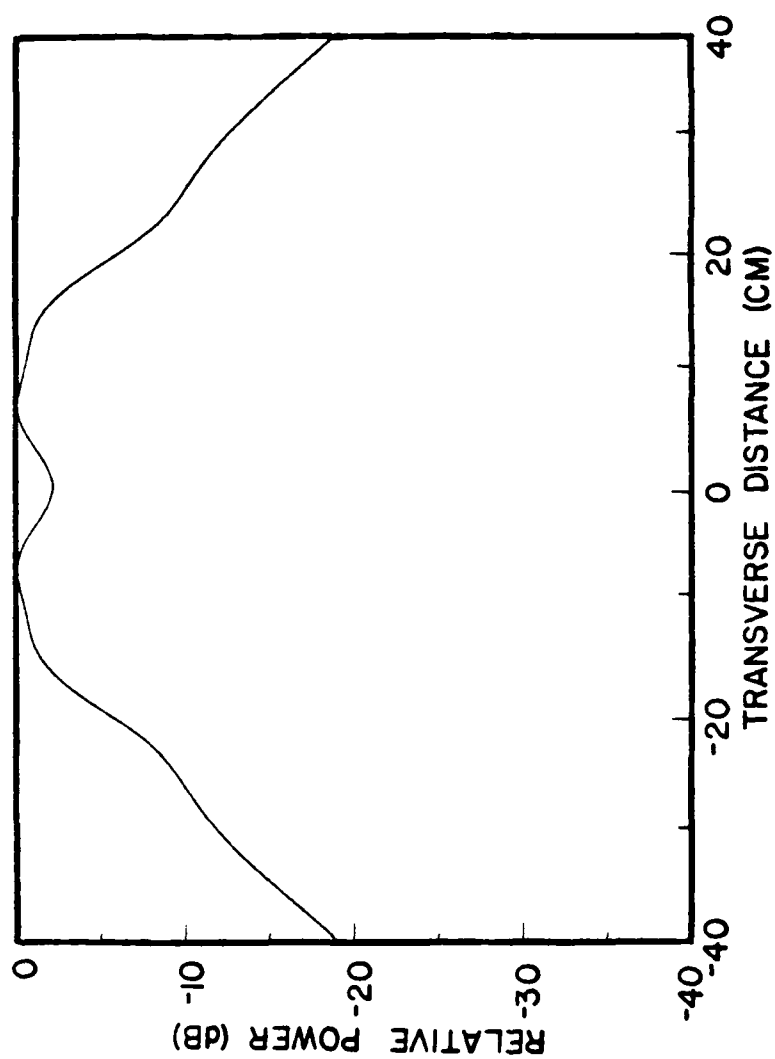


Figure 3. Non-random near-field power distribution for the in-band frequency of 3.0 GHz for the in-band scan angle of 0 degrees.

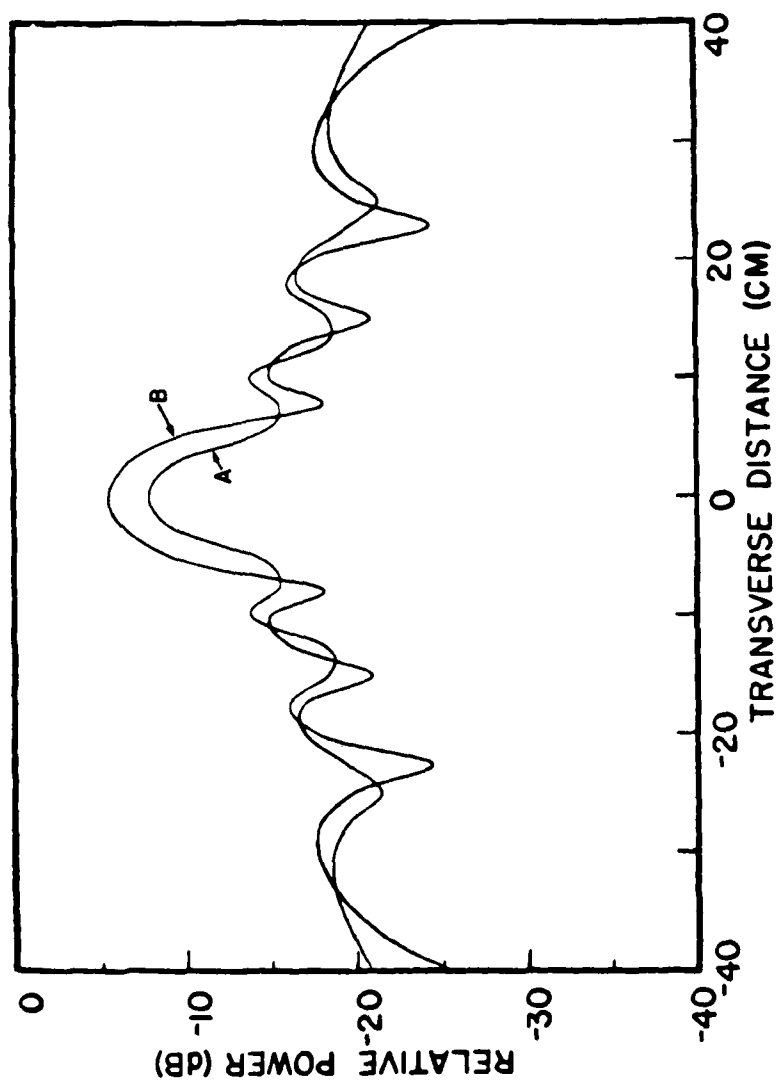


Figure 4. Intrinsic (A) and total (B) near-field covariance function of the electric field at  $y=0$  and the conjugate of the electric field at all other points on the near-field plane for the in-band frequency of 3 GHz for the in-band scan angle of 0 degrees.

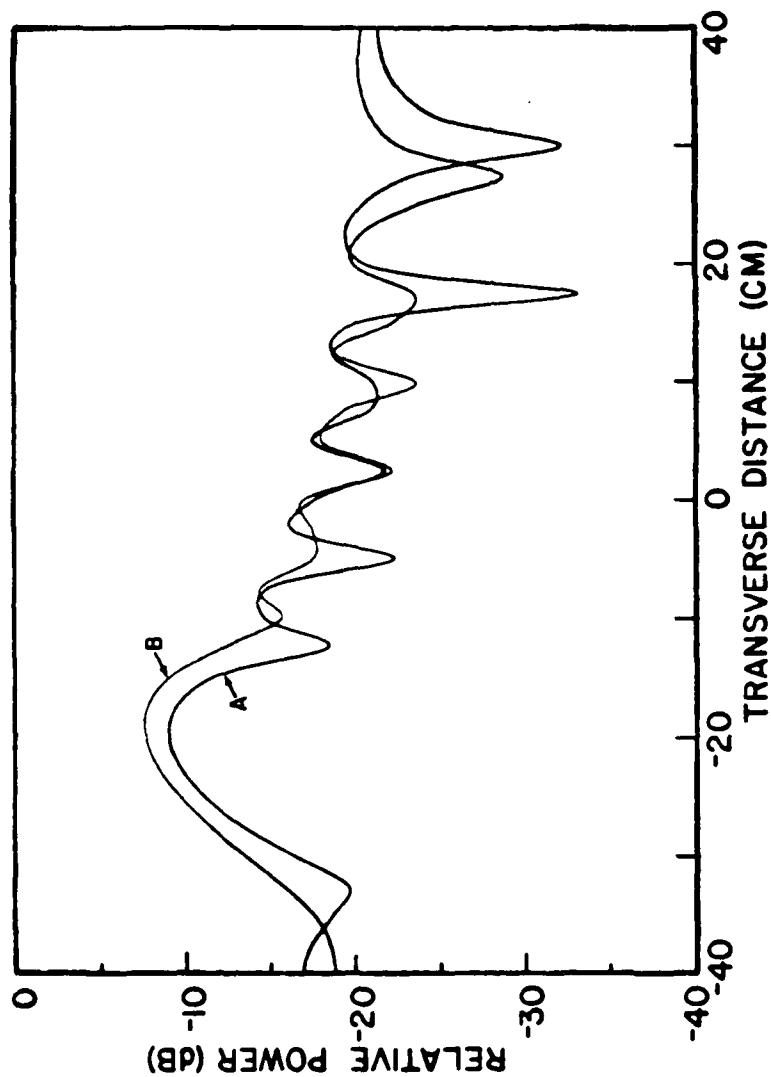


Figure 5. Intrinsic (A) and total (B) near-field covariance function of the electric field at  $y=-20$  and the conjugate of the electric field at all other points on the near-field plane for the in-band frequency of 3 GHz for the in-band scan angle of 0 degrees.

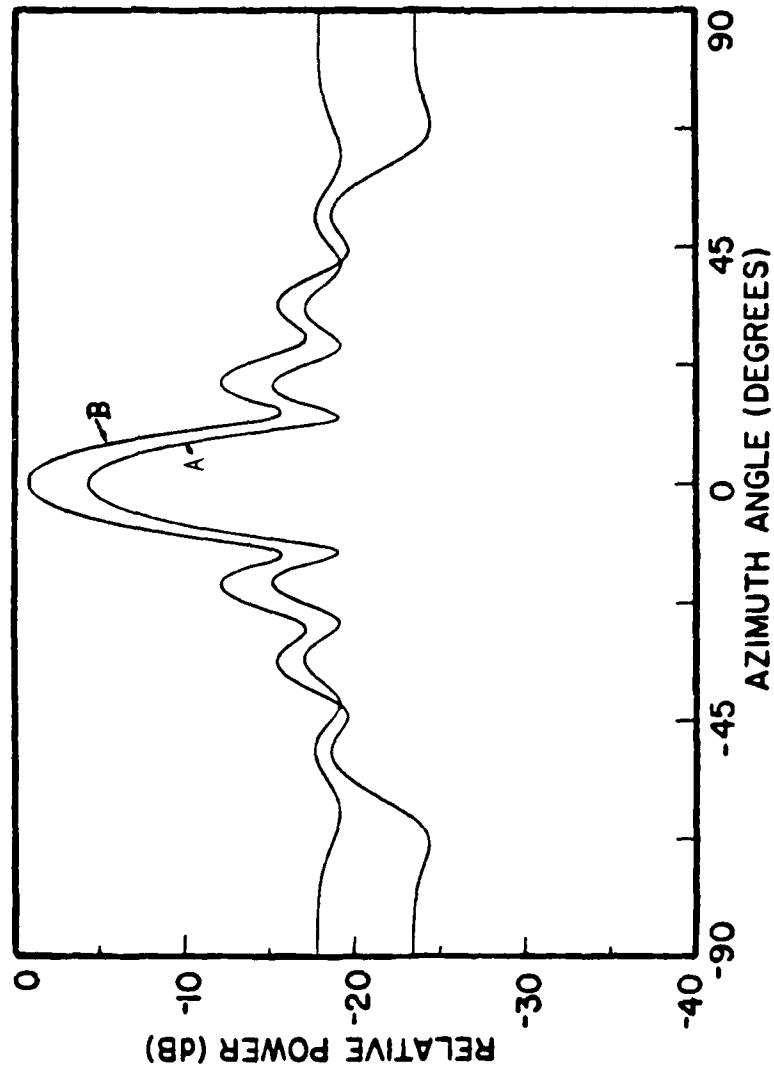


Figure 6. Analytical statistical average pattern for a nine-element dipole array of interacting (B) and non-interacting (A) elements for the in-band frequency of 3.0 GHz for the in-band scan angle of 0 degrees.

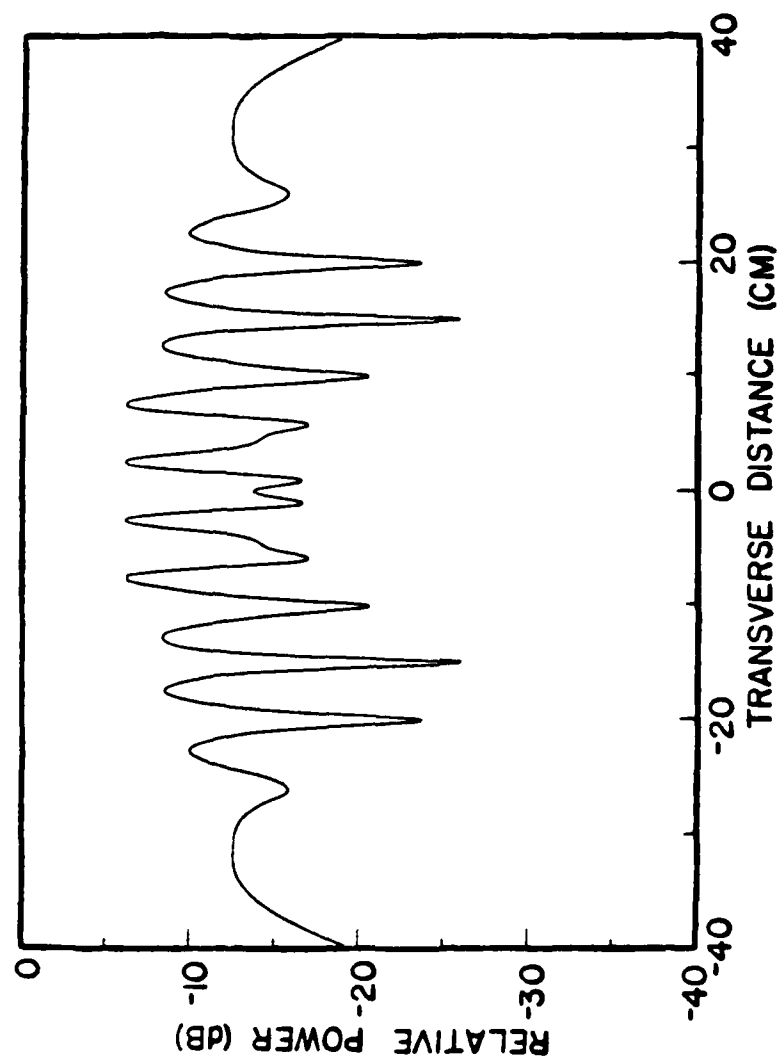


Figure 7.. Non-random near-field power distribution for the out-of-band frequency of 9.0 GHz for the in-band scan angle of 0 degrees.



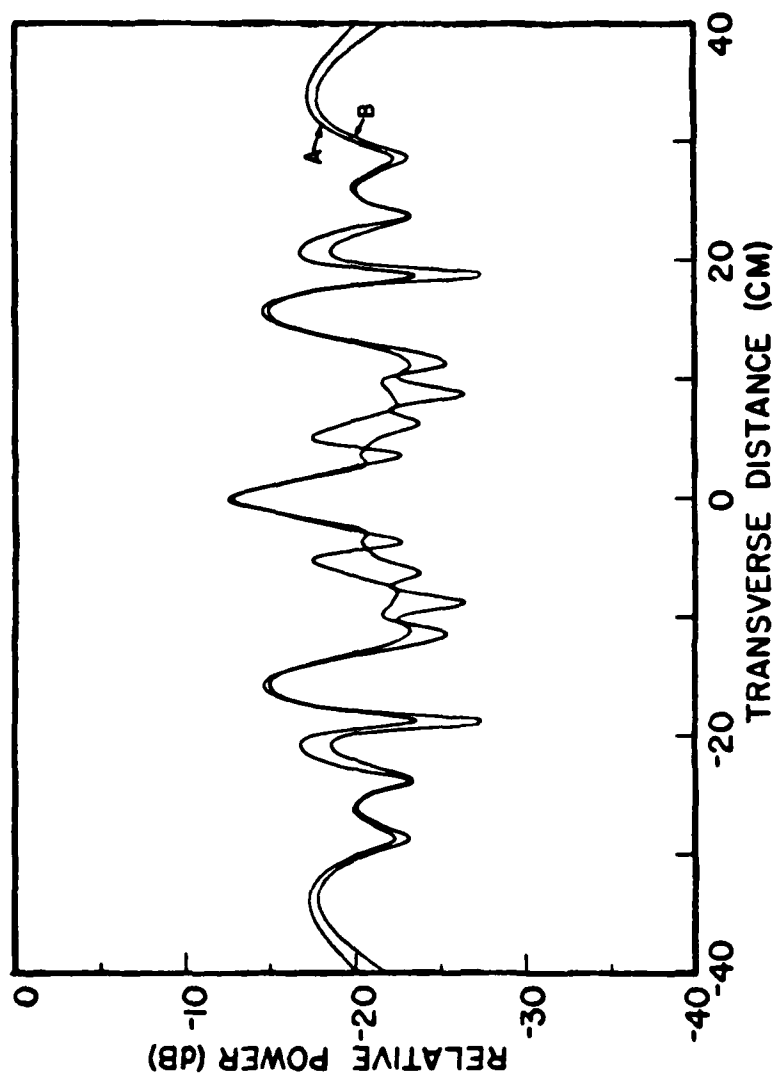


Figure 8. Intrinsic (A) and total (B) near-field covariance function of the electric field at  $y=0$  and the conjugate of the electric field at all other points on the near-field plane for the out-of-band frequency of 9 GHz for the in-band scan angle of 0 degrees.

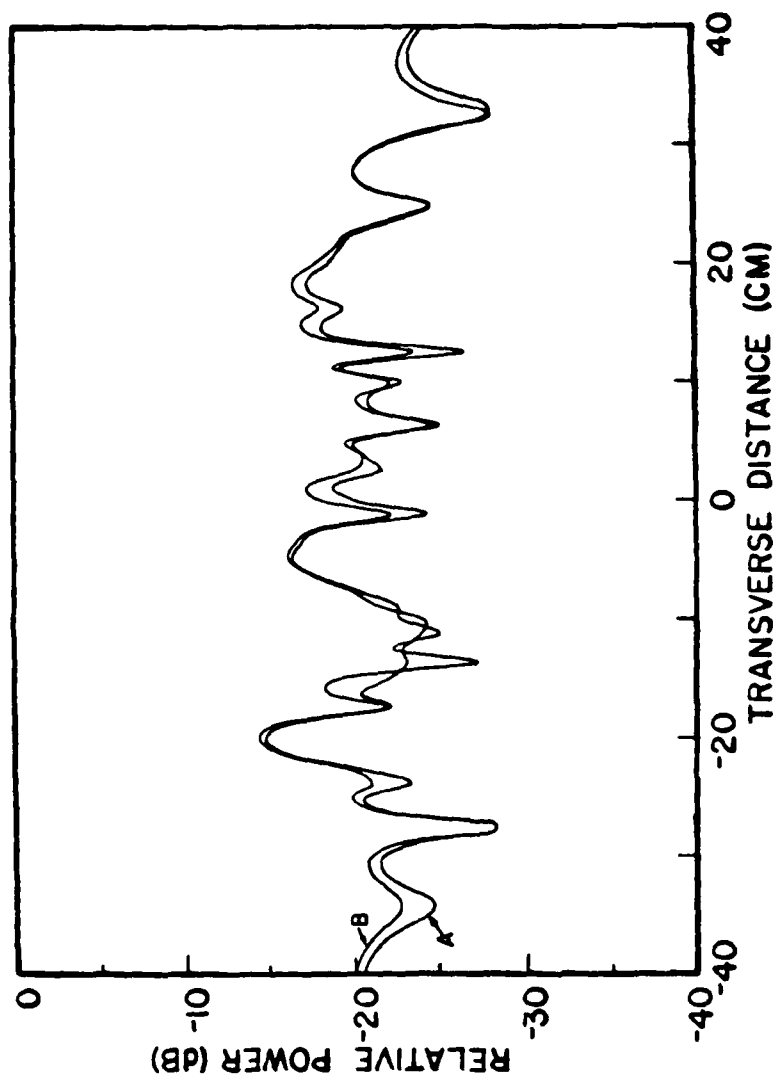


Figure 9. Intrinsic (A) and total (B) near-field covariance function of the electric field at  $y \approx -20$  and the conjugate of the electric field at all other points on the near-field plane for the out-of-band frequency of 9 GHz for the in-band scan angle of 0 degrees.

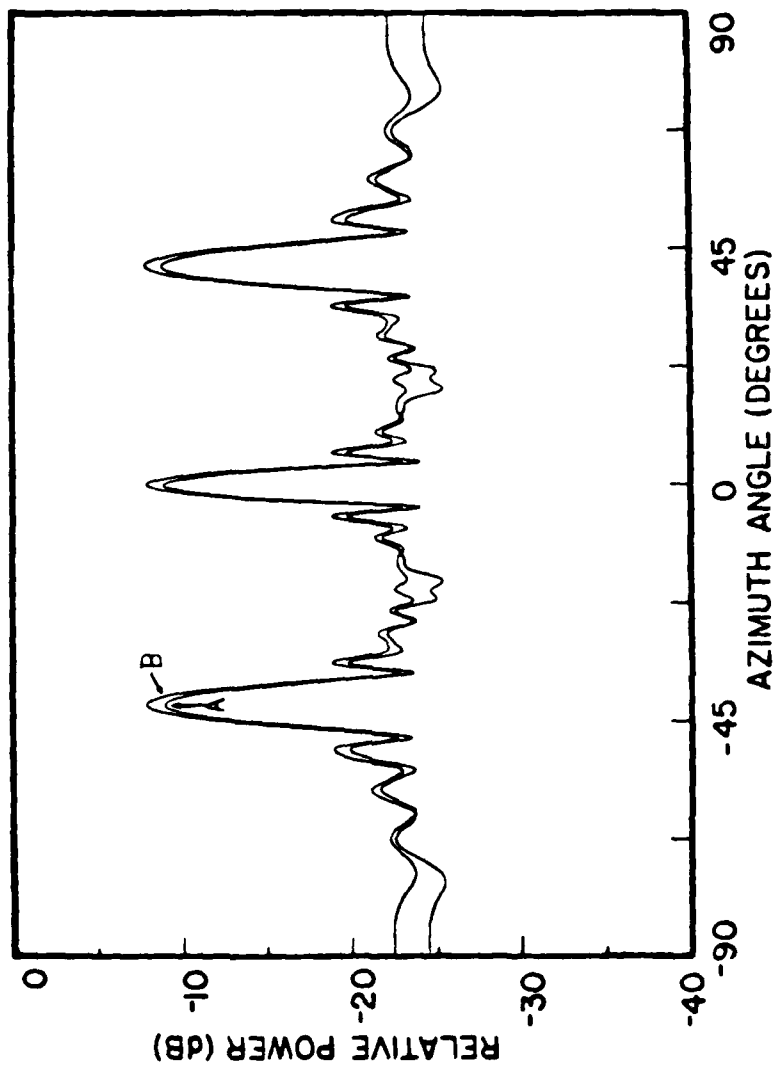


Figure 10. Analytical statistical average pattern for a nine-element dipole array of interacting (B) and non-interacting (A) elements for the out-of-band frequency of 9.0 GHz for the in-band scan angle of 0 degrees.

interacting (coupled) array elements and non-interacting (isolated) array elements by the plots labeled B and A, respectively. All of the plots in Figures 4 through 10 are normalized with respect to the peak magnitude of the non-random, in-band, near-field power distribution shown in Figure 3.

The general behavior of the near-field covariance functions may be discerned from Figures 4 and 5 for the in-band frequency and Figures 8 and 9 for the out-of-band frequency. The covariance functions for the center sample point with all other points are symmetric about the center point, while the covariance functions for a sample point opposite the edge of the array with all other sample points are asymmetrical. This behavior is expected because the array is finite. An infinite array would everywhere have a symmetrical covariance function. The total covariance function has greater peak magnitude than the intrinsic covariance, and also has broader lobes. These differences are more pronounced for the in-band frequency. This is reasonable because the current elements are only weakly coupled at 9 GHz. Accordingly, the interactive covariance component of the total covariance is much smaller than the intrinsic covariance component and, hence the total and intrinsic covariances do not differ markedly at 9.0 GHz.

The behavior of the statistical average far-field power patterns may be examined via the plots shown in Figure 6 for 3.0 GHz and Figure 10 for 9.0 GHz. The statistical average patterns for the array of interacting current elements have greater peak magnitude and decrease more rapidly versus azimuth angle than the average patterns for the array of non-interacting current elements. The difference in the average patterns for interacting and non-interacting elements is more pronounced for the in-band frequency than for the out-of-band frequency. This result could have been anticipated from the near-field covariance functions because the total and intrinsic near-field covariances are significantly different for 3.0 GHz but are only slightly different for 9.0 GHz. The results for other scan angles not displayed herein are entirely consistent with the results for the broadside scan angle.

It can be inferred from these results that the intrinsic covariance function is a "good" engineering approximation to the total covariance function if the inter-element coupling is "sufficiently" weak. The intrinsic covariance function can be accurately estimated via conventional matrix manipulations involving the measurement-derived self-covariance (variance) of the electric field at each near-field sample point and the free space Green functions. The calculated average far-field power patterns will be accurate if the coupling is "sufficiently" weak. Further numerical studies would be needed to determine whether the inter-element coupling for multimoding out-of-band waveguide phased arrays is "sufficiently" weak to permit accurate calculations of the average far-field power patterns in this manner.

### SECTION III

#### NEAR-FIELD ANTENNA-ANTENNA COUPLING

##### A. Introduction

An exact analysis of the coupling between real-world cosited antennas would be extremely difficult or perhaps impossible to achieve. Accordingly, the efforts on this task have been devoted to deriving approximate but accurate coupling prediction equations. Three different techniques for coupling analysis are under investigation. These three techniques are denoted respectively as (1) Spherical Wave (SW), (2) Plane Wave Spectrum (PWS), and (3) the Geometrical Theory of Diffraction (GTD). Most of the research efforts thus far have been devoted toward development of the SW and PWS techniques. Multiple scattering effects are not addressed in the analysis. However, multiple scattering effects can be approximately analyzed if the scattering matrix of each antenna is known from theory or measurements. Theory and equations for the SW and PWS approaches are presented and discussed in Subsection B and C, respectively. Preliminary results of numerical simulations for PWS approach are also presented in Subsection C. The GTD technique for deterministic antenna analysis has a substantial literature which can be used to derive GTD antenna coupling models [2,3]. Efforts to extend the technique to out-of-band stochastic antenna coupling problems have been initiated on this task only recently. Accordingly, discussions of GTD technique will not be included herein.

##### B. Spherical Wave Analysis

The coupling between two near-field reflector antennas is considered for arbitrary orientation and arrangement of the reflectors. Sketches showing geometric variables pertaining to the orientation and arrangements are depicted in Figures 11 and 12, where the symbols are defined as

$\vec{R}$  = vector from center of Antenna A to center  
of Antenna B,

$\vec{R}'$  = vector from the center of Antenna A to a  
specified near-field point,

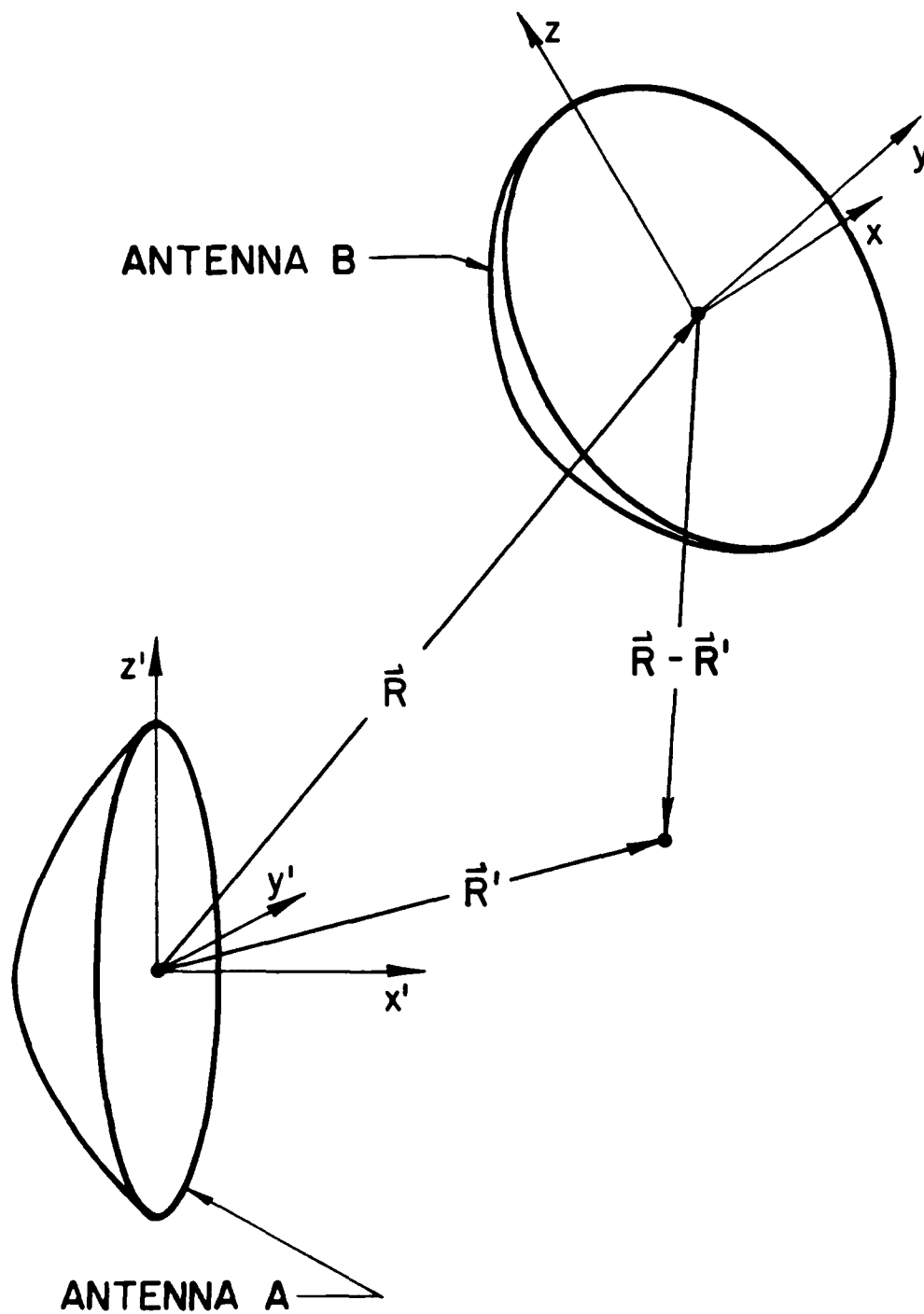


Figure 11. Sketch depicting two arbitrarily oriented near-field antennas and geometric parameters.

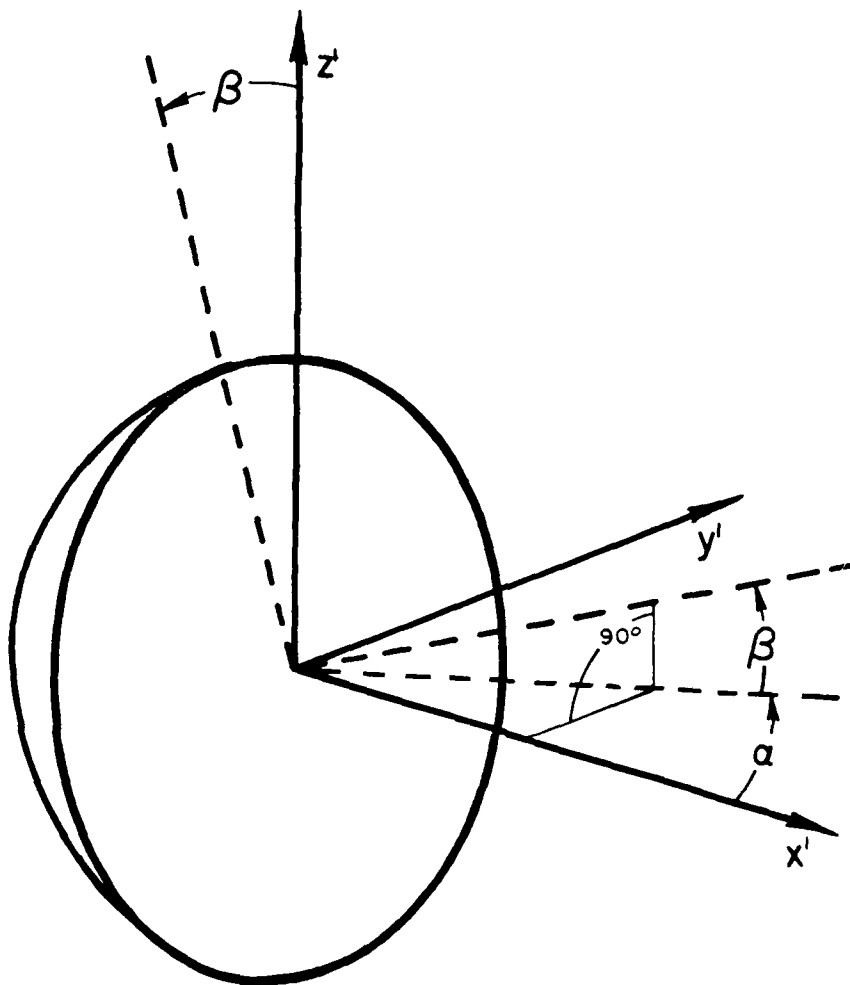


Figure 12. Sketch depicting the azimuth rotation angle  $\alpha$  and the elevation rotation angle  $\beta$ .



$\bar{R}-\bar{R}'$  = vector from the center of Antenna B  
to the specified near-field point,

$\alpha$  = azimuth rotation angle between Antenna A  
and Antenna B, and

$\beta$  = elevation rotation angle between Antenna A  
and Antenna B.

The complex voltage response  $V(\bar{R}, \alpha, \beta)$  of Antenna B when illuminated  
by Antenna A can be written as

$$V(\bar{R}, \alpha, \beta) = C_0 \cdot \int_{S'} \bar{E}^b(\bar{R}-\bar{R}' | \alpha, \beta) \cdot \bar{E}^a(\bar{R}') dS' \quad (13)$$

where  $C_0$  is a frequency dependent factor and where  $\bar{E}^a$  and  $\bar{E}^b$  denote the  
complex near-field electric fields of Antenna A and Antenna B, respectively.  
The surface integral in Equation (13) is integrated over the surface of  
the sphere of radius  $R'$ .

The vertically-polarized and horizontally polarized components of the  
electric field of Antenna A on the sphere of radius  $\bar{R}'$  centered at Antenna  
A may be computed as

$$E_v^a(R', \theta', \phi') = \sum_m \sum_n A_{mn}^v h_n^{(2)}(KR') L_{nm}(\cos \theta') e^{-jm\phi'} \quad (14)$$

for vertical polarization and

$$E_h^a(R', \theta', \phi') = \sum_m \sum_n A_{mn}^h h_n^{(2)}(KR') L_{nm}(\cos \theta') e^{-jm\phi'} \quad (15)$$

for horizontal polarization. The symbol  $h_n^{(2)}$  denotes the spherical Hankel  
function of the second kind and order  $n$ , and the symbol  $L_{nm}$  denotes the  
associated Legendre polynomial of the first kind of order  $n$  and degree  $m$ .  
The coefficients  $A_{mn}^v$  and  $A_{mn}^h$  are readily computed if  $E_v^a$  is known on any  
spherical surface. It is assumed that vertically-polarized and horizontally-  
polarized far-field patterns are known, and consequently, the coefficients

can be computed from them. Equations analogous to Equations (14) and (15) can be written for the vertically-polarized and horizontally-polarized fields of Antenna B, and a coordinate transformation can be applied to refer the fields of Antenna B to the Antenna A coordinates or vice versa. Finally, the integral can be computed numerically.

The spherical wave technique has the desirable attribute of being applicable to arbitrary arrangements and orientations of a near-field antenna pair. However, it is very expensive to use. Computer run times would be measured in hours for a complete set of angular orientations at a fixed separation distance. Accordingly, numerical simulations based on the SW technique are not presently included in the task plan.

### C. Plane Wave Spectrum Analysis

The Plane Wave Spectrum (PWS) technique has been used on this task to analyze the coupling of near-field antennas arranged as shown in Figure 13. Equations have been derived to predict the coupling for situations where one antenna is in the forward half-plane of the other and the relative rotation angles  $\alpha$  and  $\beta$  both have magnitudes  $\leq 70$  degrees. These restrictions can possibly be relaxed through further study.

The complex voltage  $V(\vec{R}, \alpha_p, \beta_q)$  induced in Antenna B when illuminated by Antenna A is derived from PWS analysis as

$$V(\vec{R} | \alpha_p, \beta_q) = c_0 \sum_m \sum_n \bar{A}(k_{ym}, k_{zn}) \bar{B}(k_{ym} - k_{yp}, k_{zn} - k_{zq}) \exp [-j \vec{k}_{mn} \cdot \vec{R}] \quad (16)$$

where

$\bar{A}(k_{ym}, k_{zn})$  = transverse vectorial plane wave spectra of Antenna A,

$\bar{B}(k_{ym} - k_{yp}, k_{zn} - k_{zq})$  = shifted transverse vectorial plane wave spectra of Antenna B,

$k_{ym} = m^{th}$  value of  $k_y$  in the range  $-k_0 \leq k_y \leq k_0$ ,

$k_{zn} = n^{th}$  value of  $k_z$  in the range  $-k_0 \leq k_z \leq k_0$ ,

$k_{yp} = p^{th}$  value of  $k_y$  in the range  $-k_0 \leq k_y \leq k_0$ ,

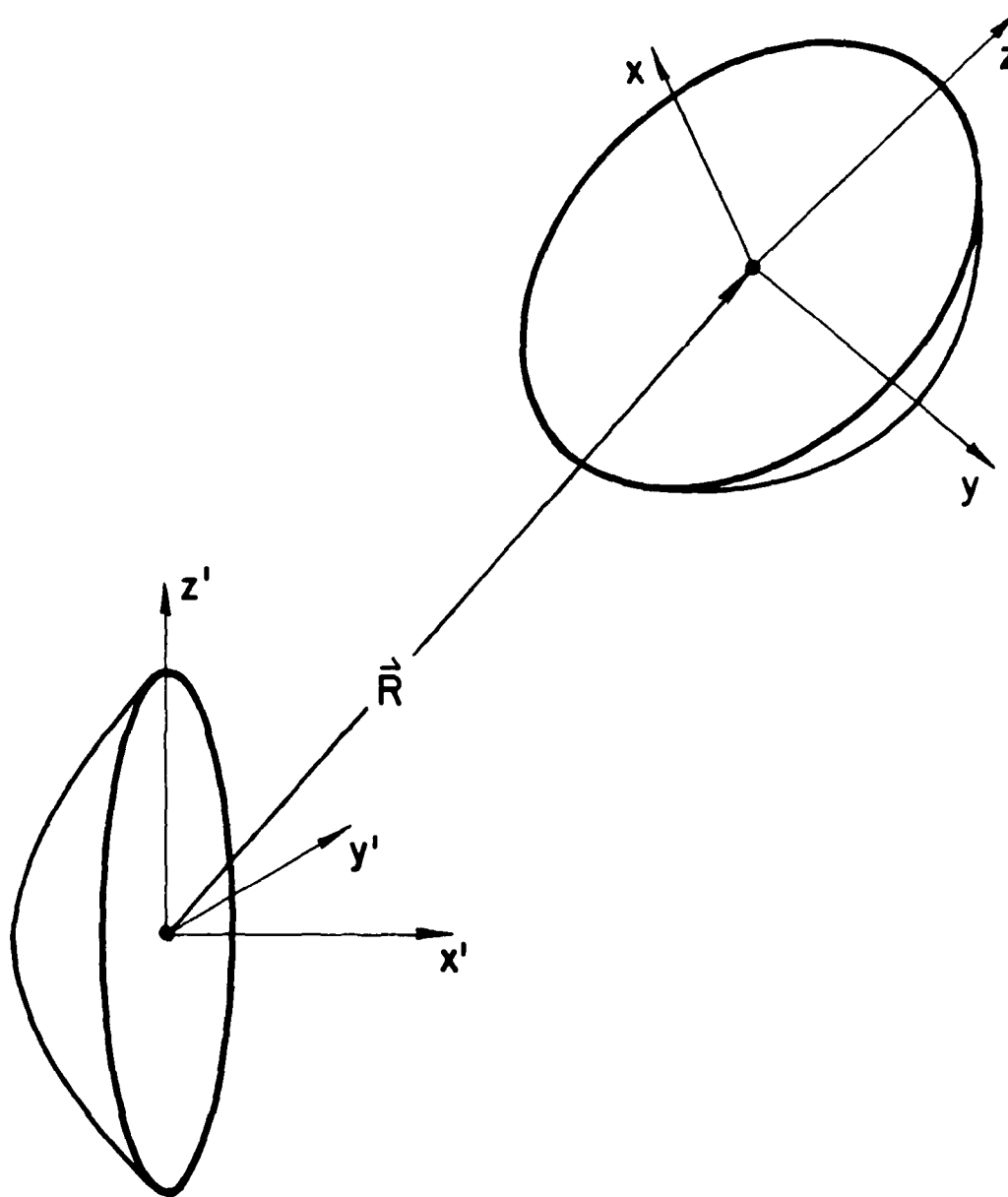


Figure 13. Sketch depicting the arrangement of two antennas appropriate for the PWS analysis of coupling.

$k_{zq} = q^{\text{th}}$  value of  $k_z$  in the range  $-k_o \leq k_z \leq k_o$ ,

$\bar{k}_{mn} = k_{xmn} \hat{x} + k_{ymn} \hat{y} + k_{zmn} \hat{z}$ , where  $k_{xmn}^2 = k_o^2 - k_{ymn}^2 - k_{zmn}^2$   
and the  $\hat{x}$ ,  $\hat{y}$  and  $\hat{z}$  are unit vectors,

$R = X \hat{x} + Y \hat{y} + Z \hat{z}$  where  $X$ ,  $Y$ , and  $Z$  are the cartesian coordinates of the center of rotation of Antenna B relative to the center of rotation of Antenna A, and

$c_o =$  a frequency-dependent proportionality factor.

The proportionality factor  $c_o$  is independent of antenna arrangements and orientations and will be suppressed in the remaining equations. The power coupled in Antenna B is

$$P(\bar{R}, \alpha_p, \beta_q) = |V(\bar{R}, \alpha_p, \beta_q)|^2 \cdot [(0.5) \cdot \Gamma_r], \quad (17)$$

where  $\Gamma_r$  is the real part of the complex admittance at the output port.

The PWS of Antenna A may be expressed in terms of the propagating modes in the waveguide feed as

$$\bar{A}(k_{ym}, k_{zn}) = \sum_{\ell} \sum_k \sum_{\mu} a_{\mu} T(\zeta_{\ell k}) \bar{H}_{\mu}(\zeta_{\ell k}) \exp [-j(k_{ym} Y_{\ell} + k_{zn} Z_k)] \quad (18)$$

where

- $a_{\mu}$  = the complex excitation coefficient of the  $\mu$ th waveguide propagating mode,
- $T(\zeta_{\ell k})$  = optical transform, computed as  $(1/2) \cdot [1 + \cos(\zeta_{\ell k})]$ ,
- $\bar{H}_{\mu}(\zeta_{\ell k})$  = the far-field vectorial pattern of the feed horn when only the  $\mu$ th mode propagates,
- $Y_{\ell}, Z_k$  = points on the reflector aperture.

The angle  $\zeta_{\ell k}$  and the reflector aperture coordinates are depicted in Figure 14. Equation (18) can be rewritten as the sum of the reflector transverse vectorial spectra  $\bar{A}_{\mu}(k_{ym}, k_{zn})$ ,

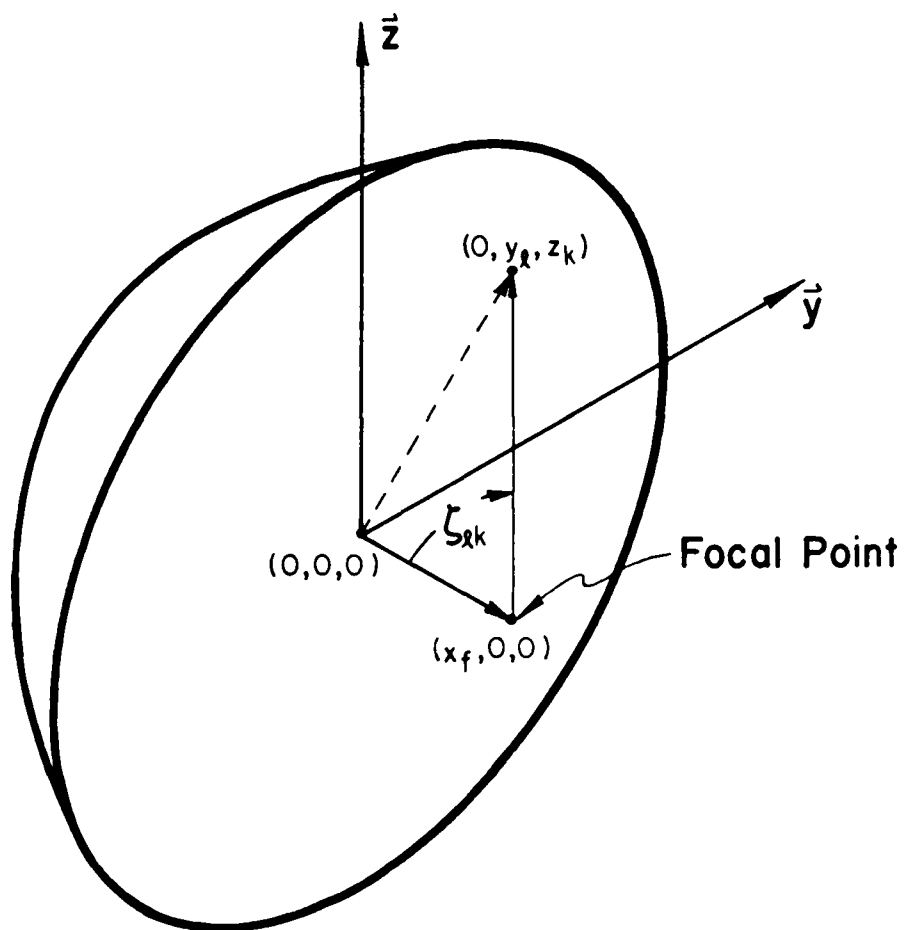


Figure 14. Sketch depicting the antenna aperture coordinates  $Y_k, Z_k$  and the optical transform angle  $l_k$ .

$$\bar{A}(k_{ym}, k_{zn}) = \sum_{\mu} a_{\mu} \bar{A}_{\mu}(k_{ym}, k_{zn}) . \quad (19)$$

The corresponding equations for the PWS of Antenna B are

$$\bar{B}(k_{ym}, k_{yn}) = \sum_{\ell} \sum_{\kappa} \sum_{\mu} b_{\mu} T(\zeta_{\ell\kappa}) \bar{H}(\zeta_{\ell\kappa}) \exp[-j(k_{ym} Y_{\ell} + k_{zn} Z_{\kappa})] \text{ and } \quad (20)$$

the alternative form,

$$\bar{B}(k_{ym}, k_{zn}) = \sum_{\mu} b_{\mu} \bar{B}_{\mu}(k_{ym}, k_{zn}) \quad (21)$$

where

$b_{\mu}$  = the complex excitation coefficient of the  $\mu^{\text{th}}$  waveguide propagating mode, and

all other symbols are as previously defined.

The equation for the statistical average power  $\langle P(\bar{R}, \alpha_p, \beta_q) \rangle$  coupled to Antenna B when illuminated by Antenna A is derived as

$$\begin{aligned} \langle P(\bar{R}, \alpha_p, \beta_q) \rangle &= \sum_m \sum_n \sum_m \sum_n \sum_{\mu} \sum_{\mu} \left\{ [\langle a_{\mu}^* \rangle \langle a_{\mu} \rangle + c_{\mu, \mu}^a] [\langle b_{\mu}^* \rangle \langle b_{\mu} \rangle + c_{\mu, \mu}^b] \right. \\ &\quad \times \bar{A}_{\mu}^*(k_{ym}, k_{zn}) \cdot \bar{B}_{\mu}^*(k_{ym}, -k_{yp}, k_{zn}, -k_{zq}) \exp[j\bar{k}_{m,n} \cdot \bar{R}] \\ &\quad \left. \times A_{\mu}(k_{ym}, k_{zn}) \bar{B}_{\mu}(k_{yn} - k_{yp}, k_{zn} - k_{zq}) \exp[-j\bar{k}_{mn} \cdot \bar{R}] \right\} \quad (22) \end{aligned}$$

where the statistical quantities are defined as

$\langle a_{\mu} \rangle$  = average value of the complex mode excitation coefficient  $a_{\mu}$ ,

$\langle b_{\mu} \rangle$  = average value of the complex mode excitation coefficient  $b_{\mu}$ ,

$C_{\mu,\mu}^a$  = covariance function for  $a_{\mu}^*$ , and  $a_{\mu}$ , and

$C_{\mu,\mu}^b$  = covariance function for  $b_{\mu}^*$ , and  $b_{\mu}$ .

The wavevector  $\bar{k}_{mn}$  is defined as  $\bar{k}_{mn} = k_{xmn} \hat{x} + k_{ymn} \hat{y} + k_{zmn} \hat{z}$ . Similarly,  $\bar{k}_{m'n'}$  is defined as  $\bar{k}_{m'n'} = k_{xm'n'} \hat{x} + k_{ym'n'} \hat{y} + k_{zn} \hat{z}$ .

Numerical simulations have been conducted to compute the power coupled between a pair of cosited antennas. The antenna arrangement is shown in Figure 15. Antenna B is displaced a longitudinal distance X and lateral distance Y from Antenna A. The antennas are not displaced in the vertical Z direction. The power coupled to Antenna B versus the rotation angle  $\alpha$  was computed for selected values of x and y for rotation angles in the range  $-30 \leq \alpha \leq +30$  degrees. Only the azimuth Plane Wave Spectrums of the antennas were used in the calculations. Calculations using the full 2-dimensional spectrum of the antennas are in progress and should be completed in the near future.

The apertures of Antenna A and Antenna B are 24 inches and 48 inches, respectively. The antennas are fed by WR-187 waveguide whose cutoff frequency for the  $TE_{20}$  mode is 6.309 GHz. The in-band operating frequency of each antenna is 5.5 GHz. Calculations were made for the in-band frequency of 5.5 GHz and the out-of-band frequency of 6.5 GHz. The power flow in each waveguide feed is entirely in the  $TE_{10}$  mode at 5.5 GHz. The  $TE_{10}$  and  $TE_{20}$  modes can both propagate at 6.5 GHz.

Antenna coupling can be conveniently described in terms of the mutual gain  $M(\bar{R}, \alpha)$  relative to a pair of isotropic radiators.  $M(\bar{R}, \alpha)$  is computed as

$$M(\bar{R}, \alpha) = \left( \frac{4\pi R}{\lambda} \right)^2 \frac{P(\bar{R}, \alpha)}{P_a}, \quad (23)$$

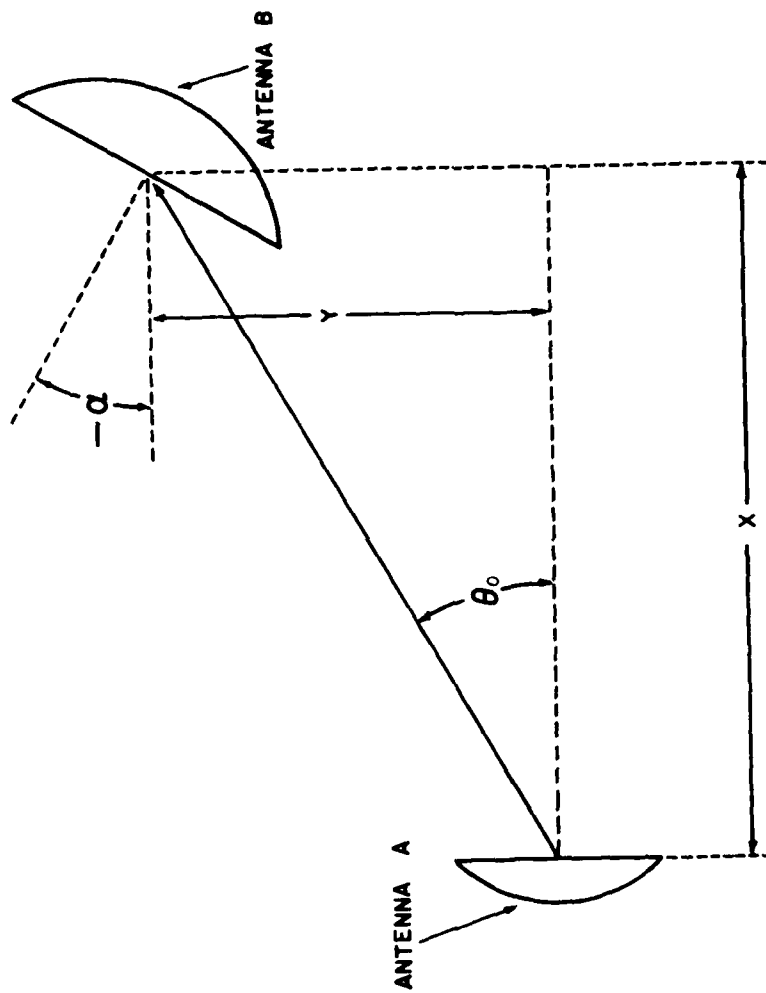


Figure 15. Sketch of the near-field arrangement of Antenna A and Antenna B used in the numerical simulations.



where  $\lambda$  is the operating wavelength and  $P_a$  is the power input to Antenna A. For the purpose of this study, a power transfer efficiency factor of 1.0 assumed for Antenna A and, hence, the total power radiated by Antenna A is assumed to equal the input power.

The in-band far-field antenna patterns of Antenna A and Antenna B are plotted in Figures 16 and 17, respectively. The estimated theoretical gain relative to an isotropic radiator is indicated at the top of each plot. The antennas were regarded as linear apertures with an "aperture efficiency" of 0.9 relative to comparable uniformly illuminated apertures for purposes of estimating the gain.

Out-of-band antenna patterns for the antennas are shown in Figures 18 through 21. Figures 18 and 20 show plots of the out-of-band far-field patterns of Antenna A and Antenna B, respectively, for equal waveguide feed power flow in the  $TE_{10}$  and  $TE_{20}$  mode with a relative phase angle of zero degrees between the modes in each feed. Figure 20 shows the out-of-band pattern for Antenna A for equal power flow in both modes with the phase of the  $TE_{20}$  mode  $+35^\circ$  relative to the  $TE_{10}$  mode. Similarly, Figure 21 shows the out-of-band pattern for Antenna B for equal power flow in both modes with the phase of the  $TE_{20}$  mode  $-50^\circ$  relative to the  $TE_{10}$  mode.

The in-band to in-band mutual gain of the antenna pair is shown in Figures 22 through 29. Each figure shows a plot of the mutual gain expressed in decibels versus the rotation angle  $\alpha$  in degrees for the indicated values of longitudinal separation distance  $X$  and transverse separation distance  $Y$ . The mutual gain relative to a pair of isotropic antennas is at the top of each plot.

The out-of-band to out-of-band mutual gain of the antenna pair is shown in Figures 30 through 37 for the modes propagating in phase. The plots are arranged in the same sequence according to the  $X$  and  $Y$  displacements as the in-band to in-band plots. Figure 38 shows the out-of-band to out-of-band mutual gain for the indicated out-of-phase modal propagation for the longitudinal separation distance of 20 feet and lateral displacement of 5 feet.

Two general trends common to the in-band to in-band and the out-of-band to out-of-band situations may be discerned from inspection of the

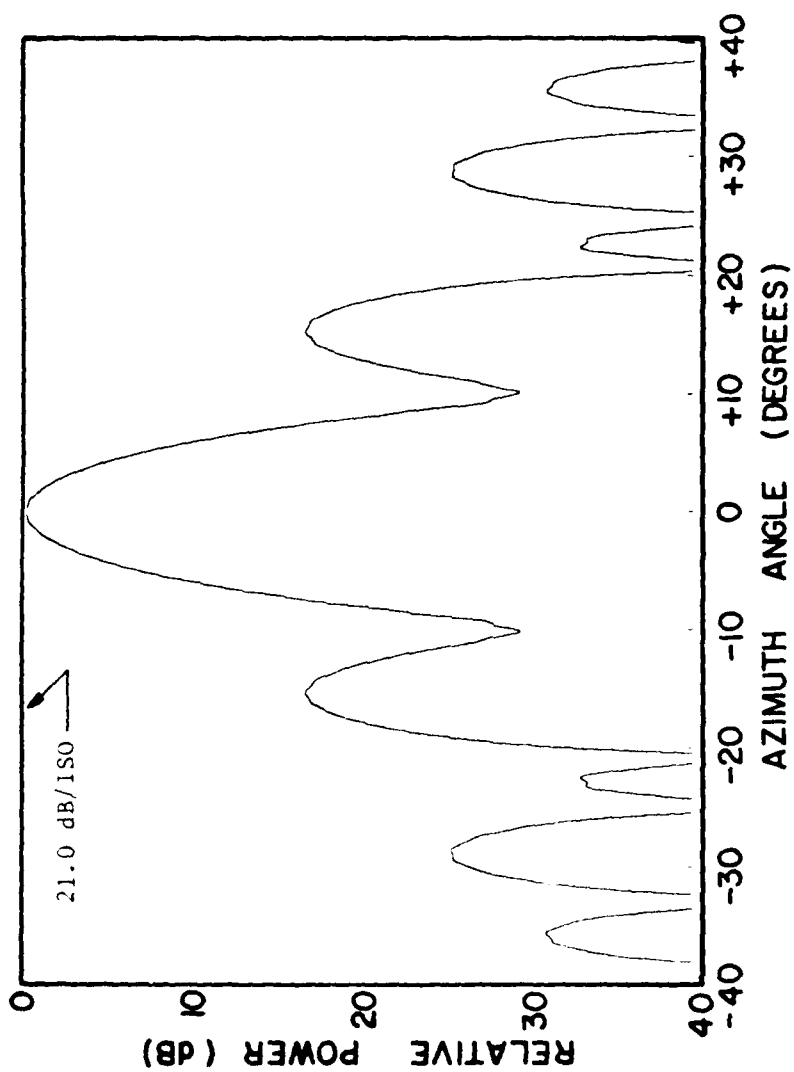


Figure 16. Far-field antenna pattern for Antenna A at the in-band frequency of 5.5 GHz for waveguide feed power flow entirely in the  $TE_{10}$  mode.

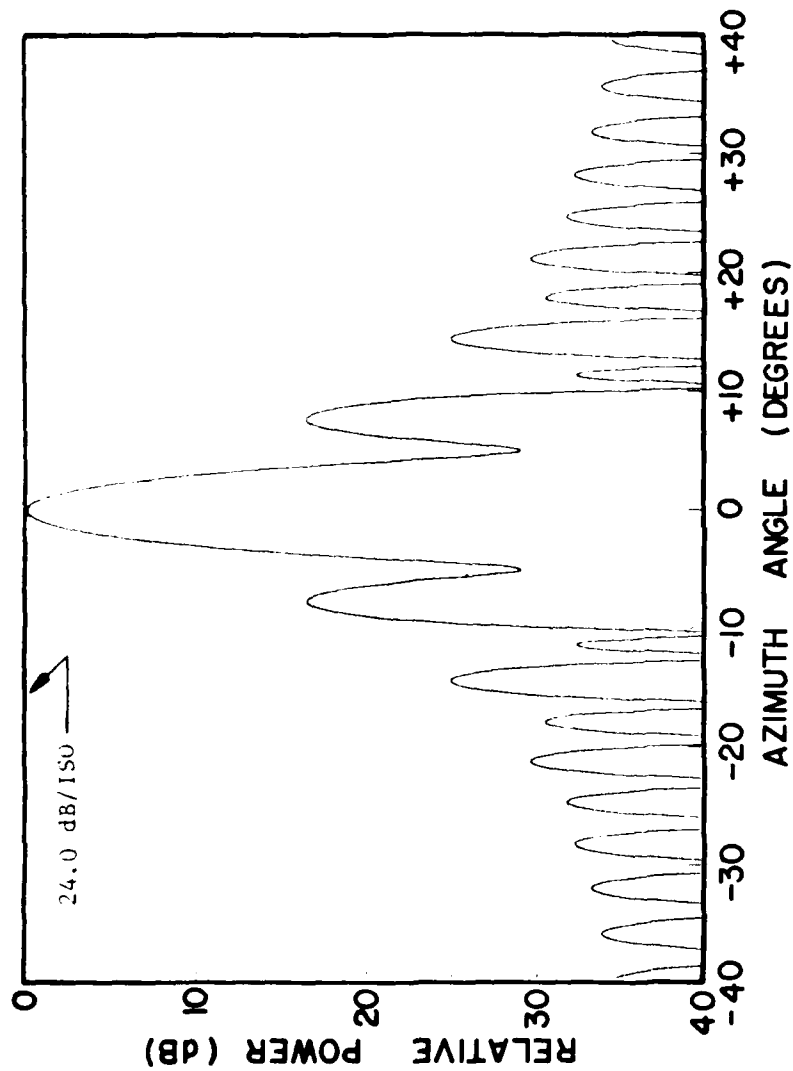


Figure 17. Far-field antenna pattern for Antenna B at the in-band frequency of 5.5 GHz for waveguide feed power flow entirely in the  $TE_{10}$  mode.

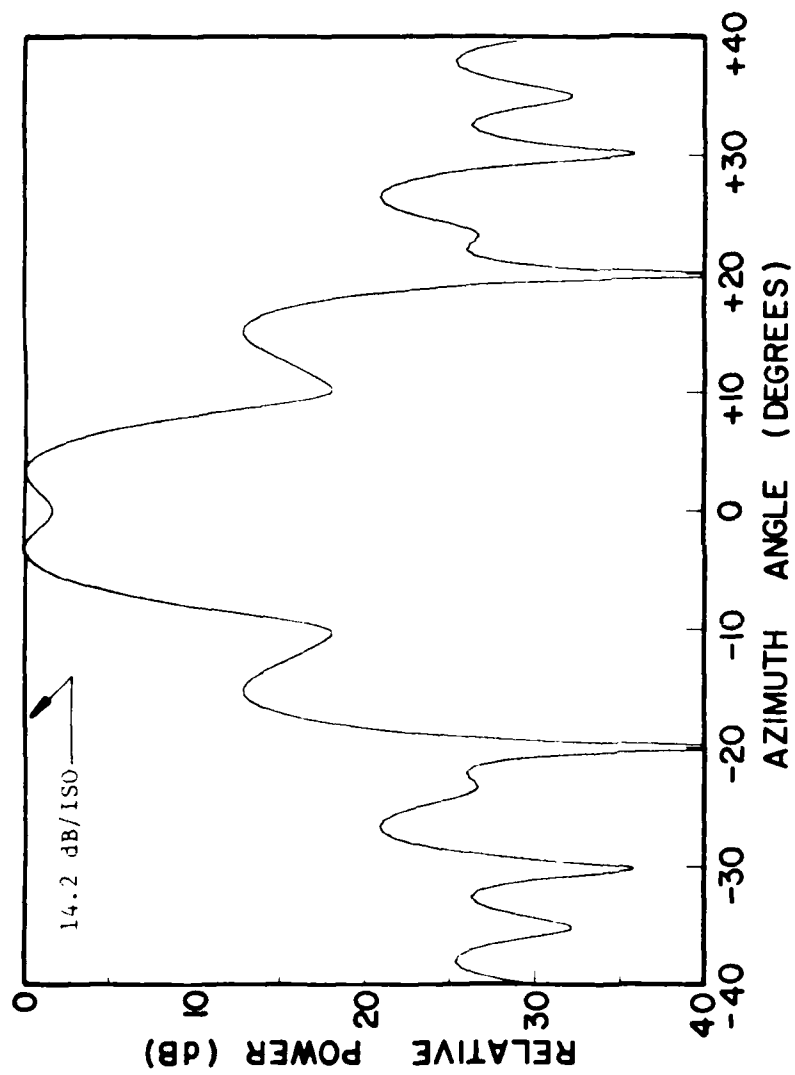


Figure 15. Far-field antenna pattern for Antenna A at the out-of-band frequency of 6.5 GHz for equal waveguide power flow in the  $TE_{10}$  and  $TE_{20}$  modes with relative phase angle of 0 degrees.

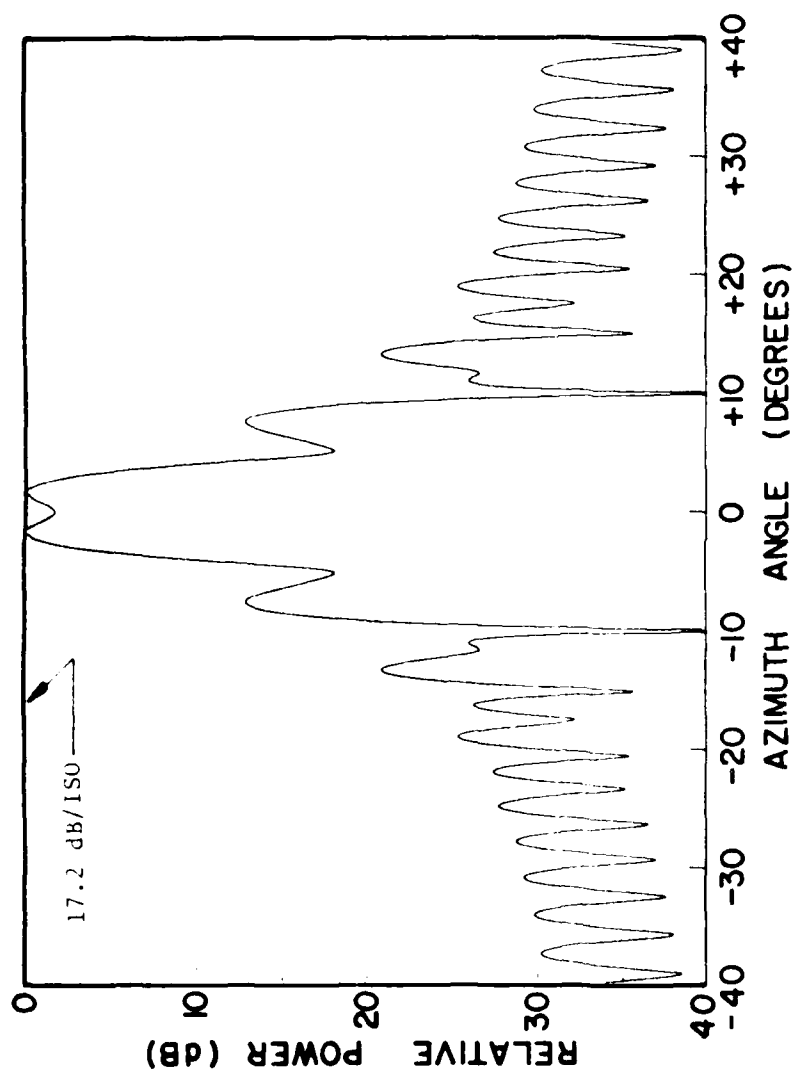


Figure 19. Far-field antenna pattern for Antenna B at the out-of-band frequency of 6.5 GHz for equal waveguide power flow in the  $TE_{10}$  and  $TE_{20}$  modes with relative phase angle of 0 degrees.

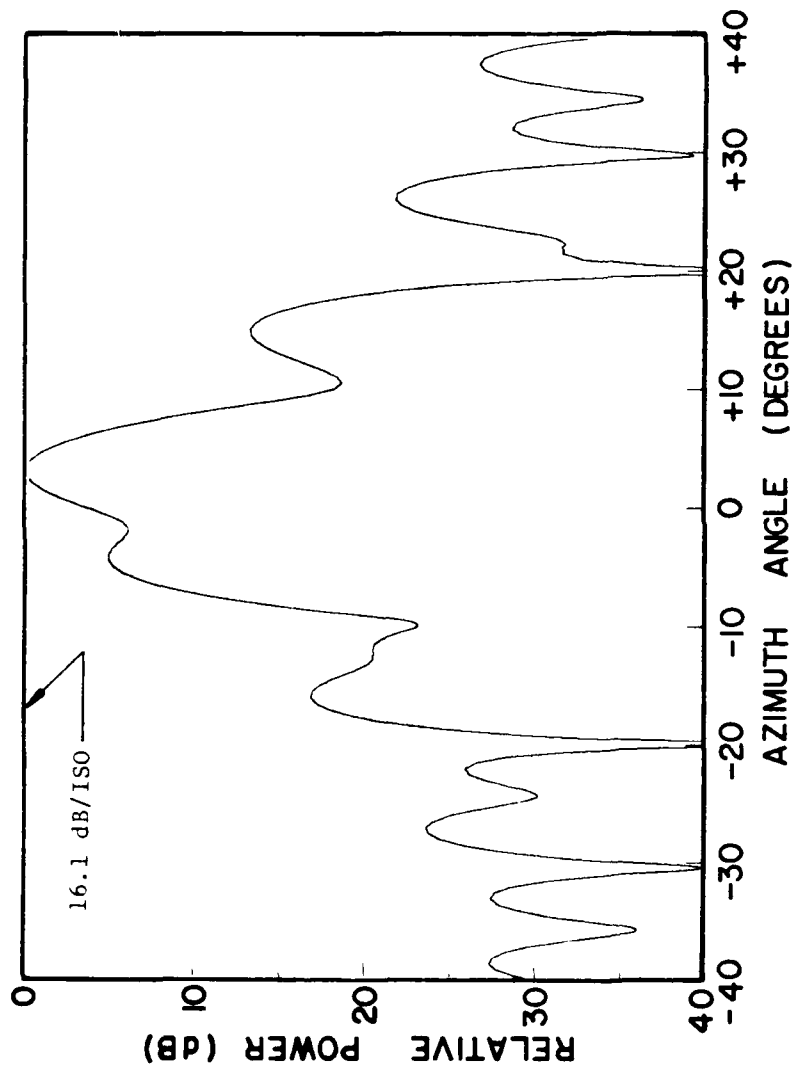


Figure 20. Far-field antenna pattern for Antenna A at the out-of-band frequency of 6.5 GHz for equal waveguide power flow in the  $TE_{10}$  and  $TE_{20}$  modes with relative phase angle of 35 degrees.

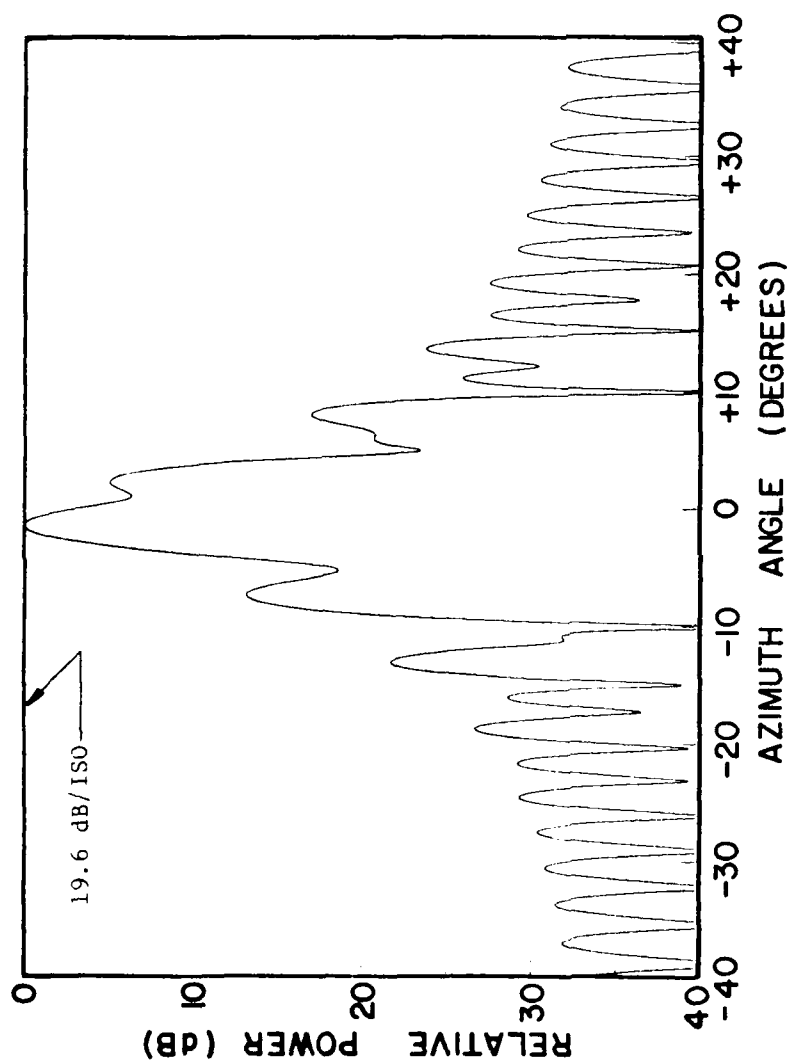


Figure 21. Far-field antenna pattern for Antenna B at the out-of-band frequency of 6.5 GHz for equal waveguide power flow in the  $TE_{10}$  and  $TE_{20}$  modes with relative phase angle of -50 degrees.

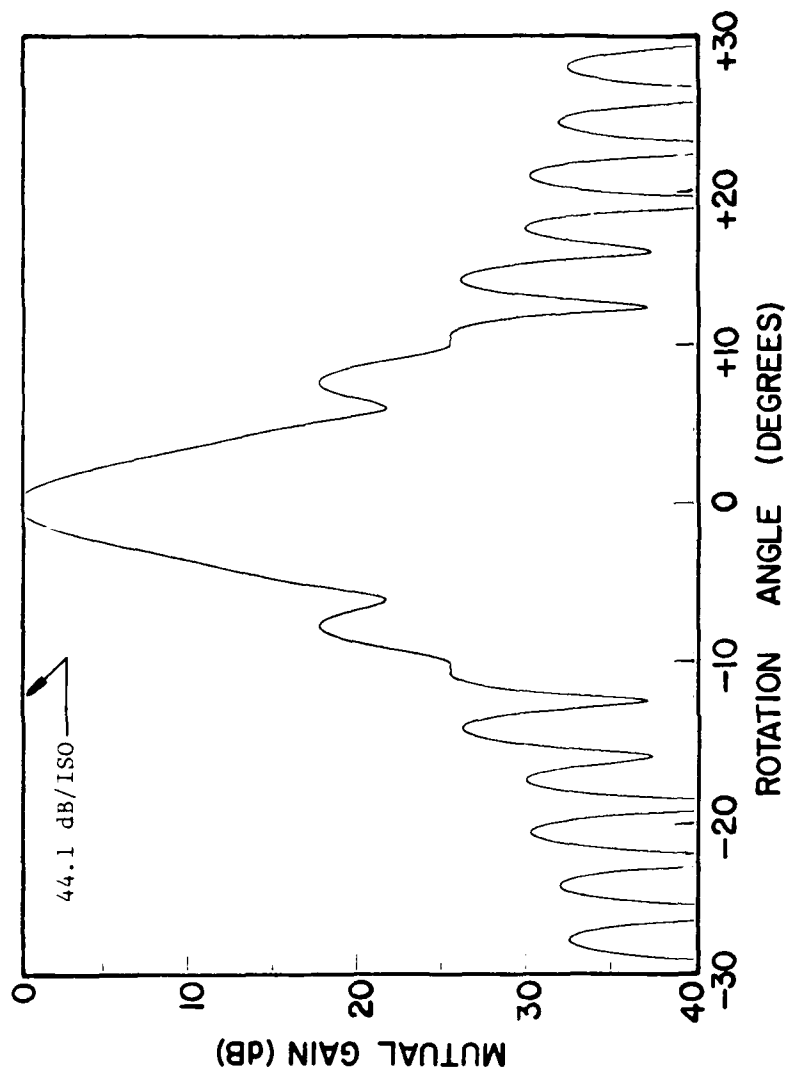


Figure 22. Mutual Gain versus rotation angle for both antennas operating in-band at 5.5 GHz for waveguide feed power flow entirely in the  $TE_{10}$  mode for the longitudinal separation distance  $X = 40$  feet and the transverse separation distance  $Y = 0$  feet.



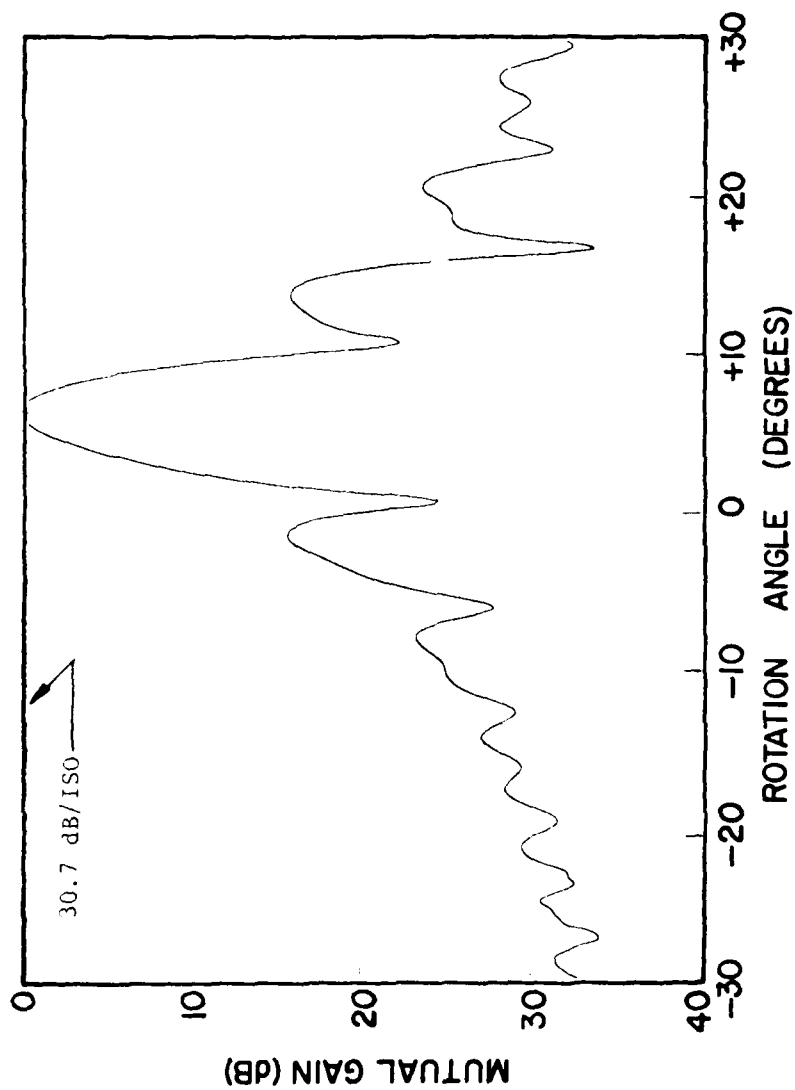


Figure 23. Mutual Gain versus rotation angle for both antennas operating in-band at 5.5 GHz for waveguide feed power flow entirely in the  $TE_{10}$  mode for the longitudinal separation distance  $X = 40$  feet and the transverse separation distance  $Y = 5$  feet.

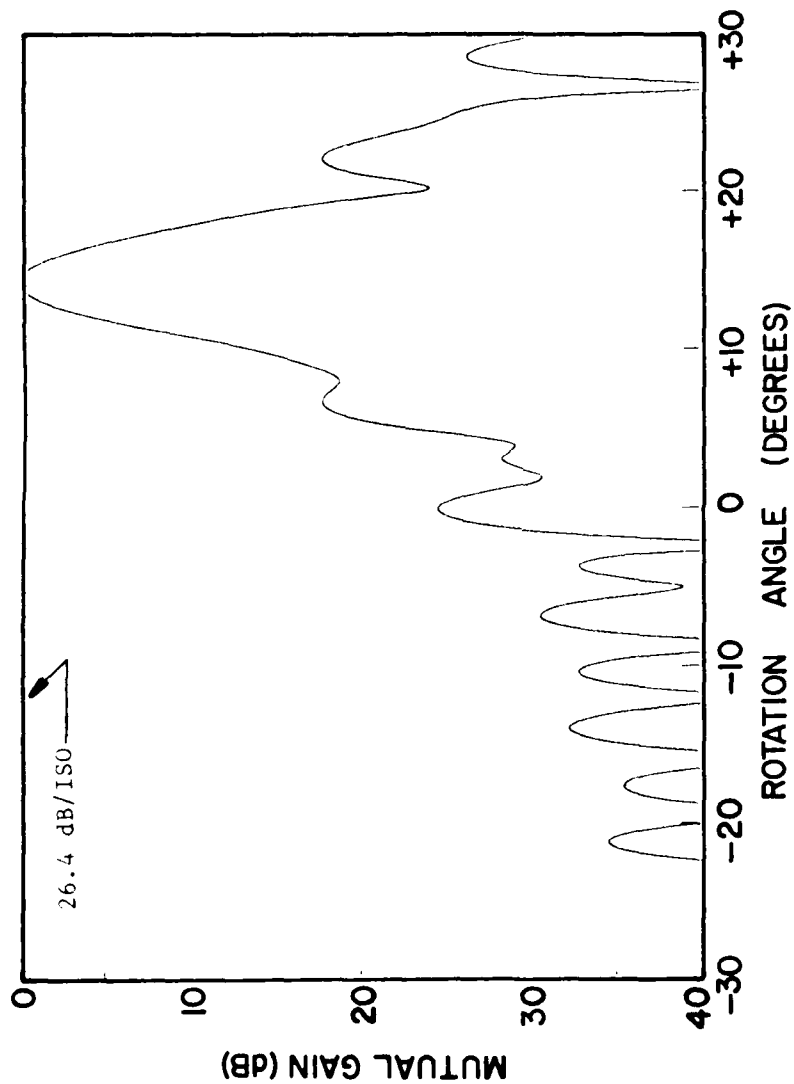


Figure 24. Mutual Gain versus rotation angle for both antennas operating in-band at 5.5 GHz for waveguide feed power flow entirely in the  $TE_{10}$  mode for the longitudinal separation distance  $X = 40$  feet and the transverse separation distance  $Y = 10$  feet.

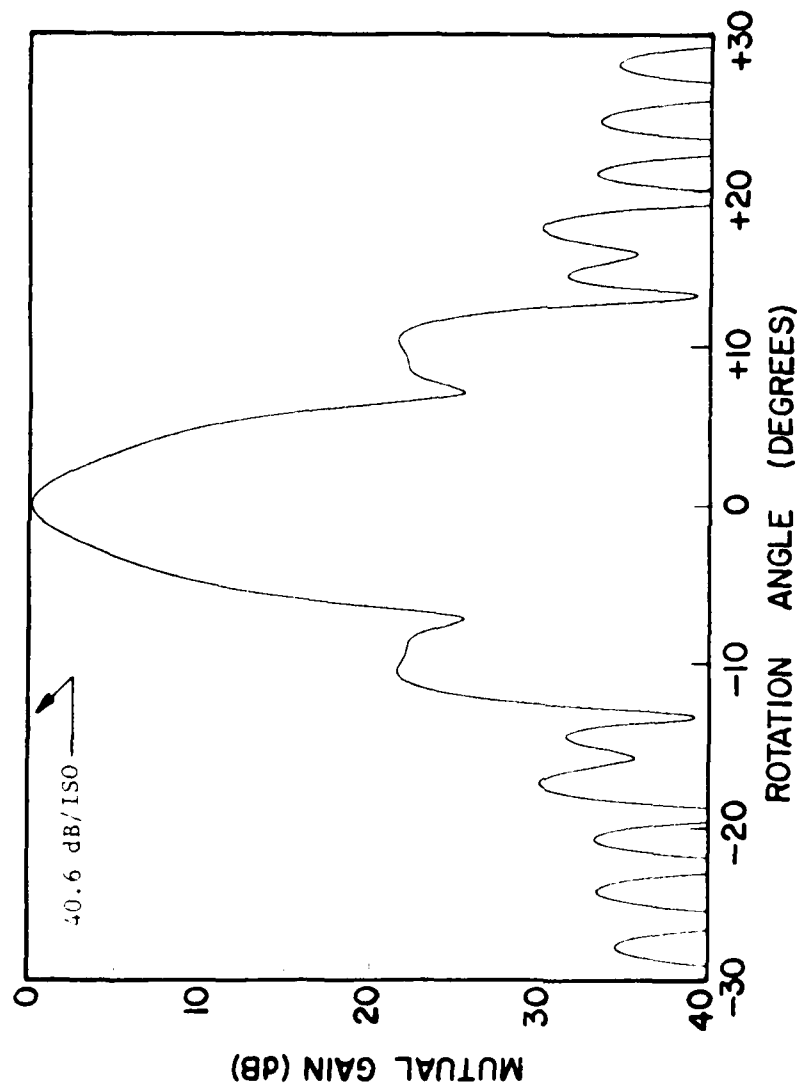


Figure 25. Mutual Gain versus rotation angle for both antennas operating in-band at 5.5 GHz for waveguide feed power flow entirely in the  $TE_{10}$  mode for the longitudinal separation distance  $X = 20$  feet and the transverse separation distance  $Y = 0$  feet.

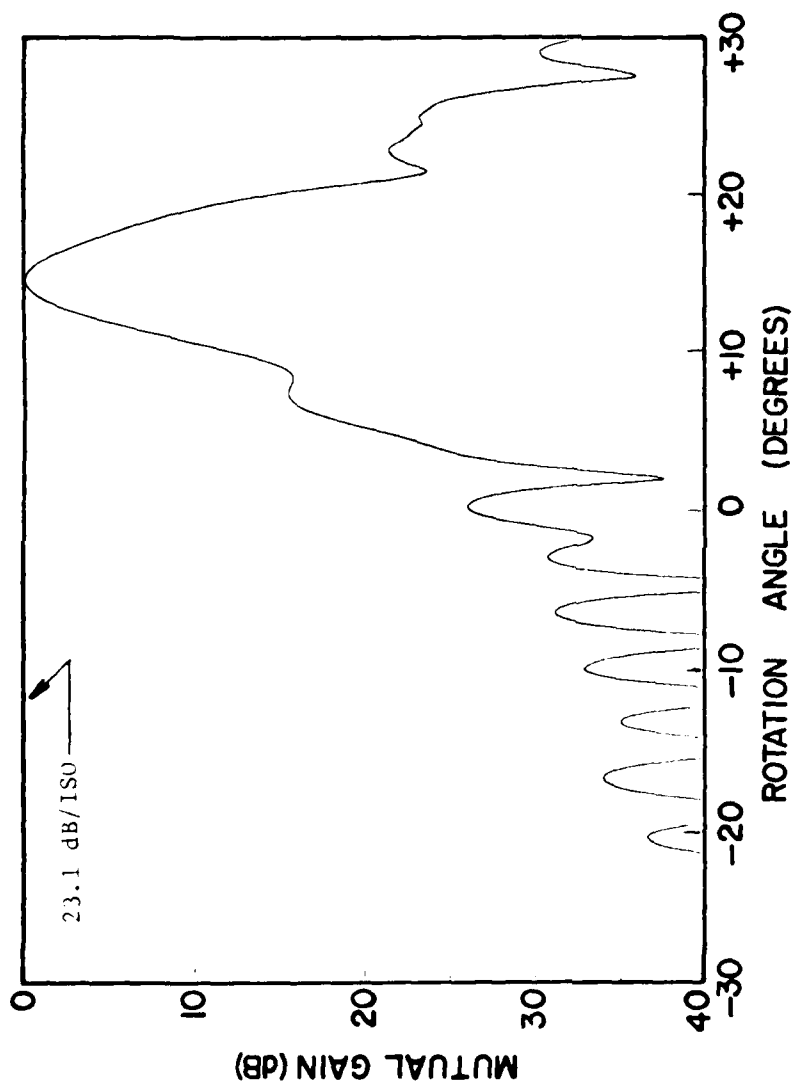


Figure 26. Mutual Gain versus rotation angle for both antennas operating in-band at 5.5 GHz for waveguide feed power flow entirely in the  $TE_{10}$  mode for the longitudinal separation distance  $X = 20$  feet and the transverse separation distance  $Y = 5$  feet.

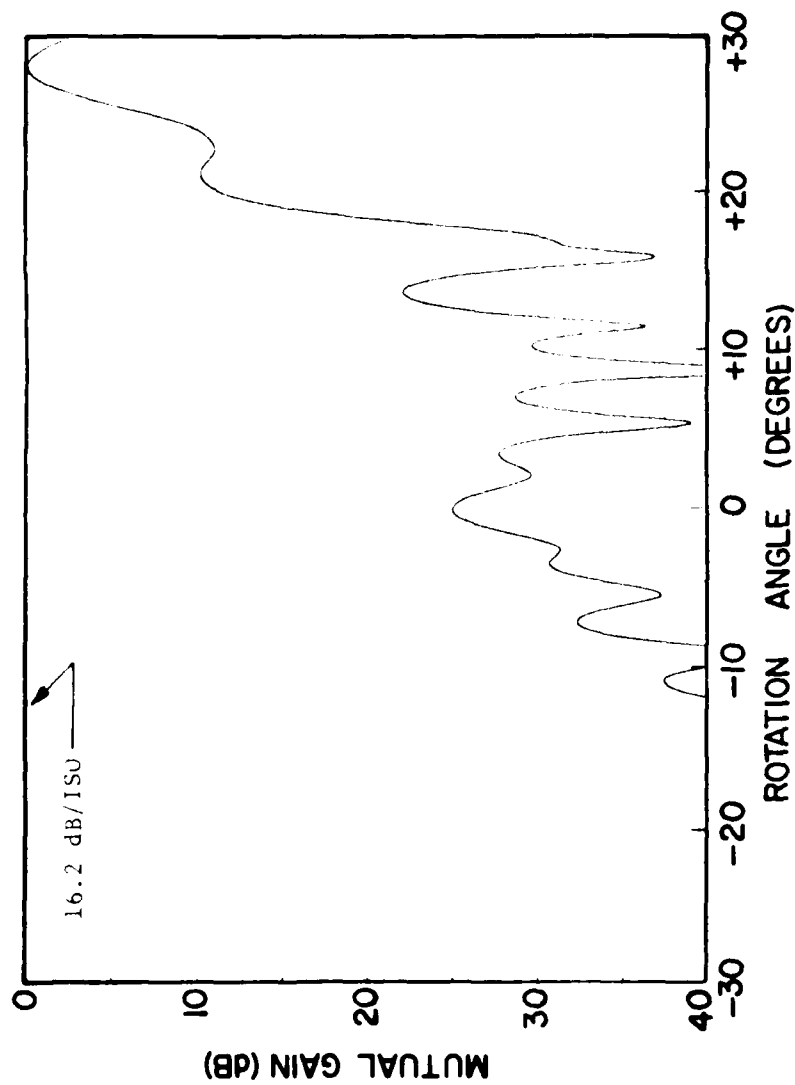


Figure 27. Mutual Gain versus rotation angle for both antennas operating in-band at 5.5 GHz for waveguide feed power flow entirely in the  $TE_{10}$  mode for the longitudinal separation distance  $X = 20$  feet and the transverse separation distance  $Y = 10$  feet.

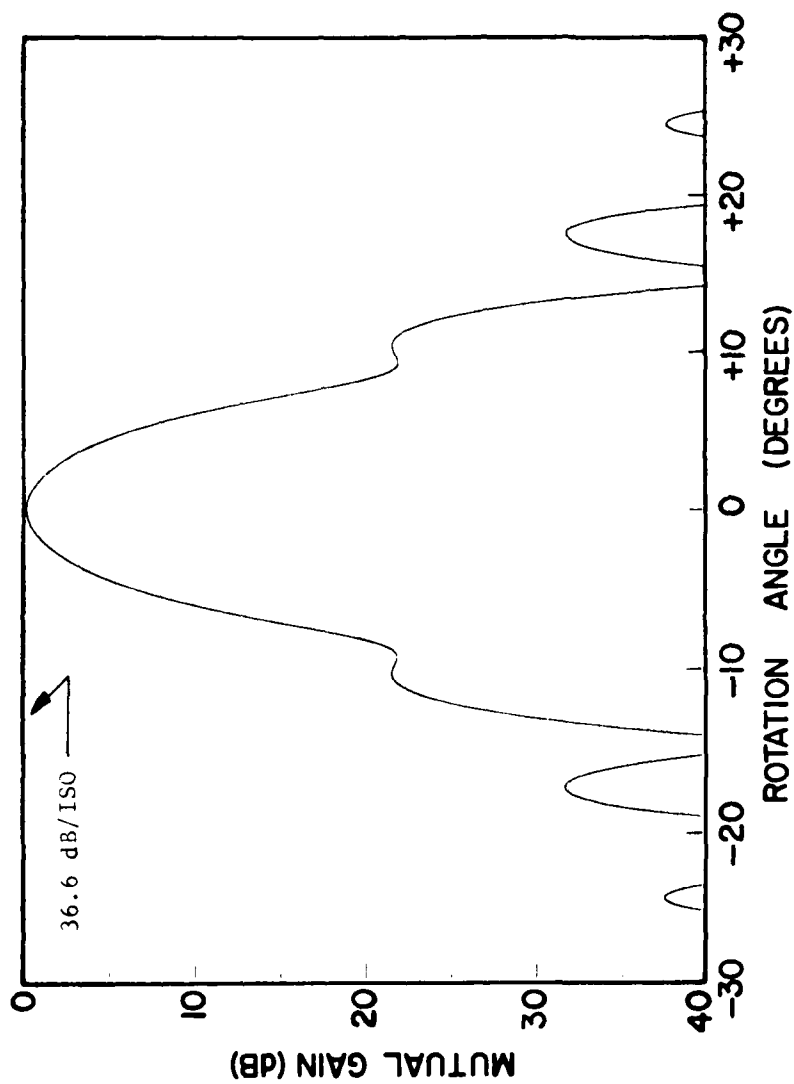


Figure 28. Mutual Gain versus rotation angle for both antennas operating in-band at 5.5 GHz for waveguide feed power flow entirely in the  $TE_{10}$  mode for the longitudinal separation distance  $X = 10$  feet and the transverse separation distance  $Y = 0$  feet.

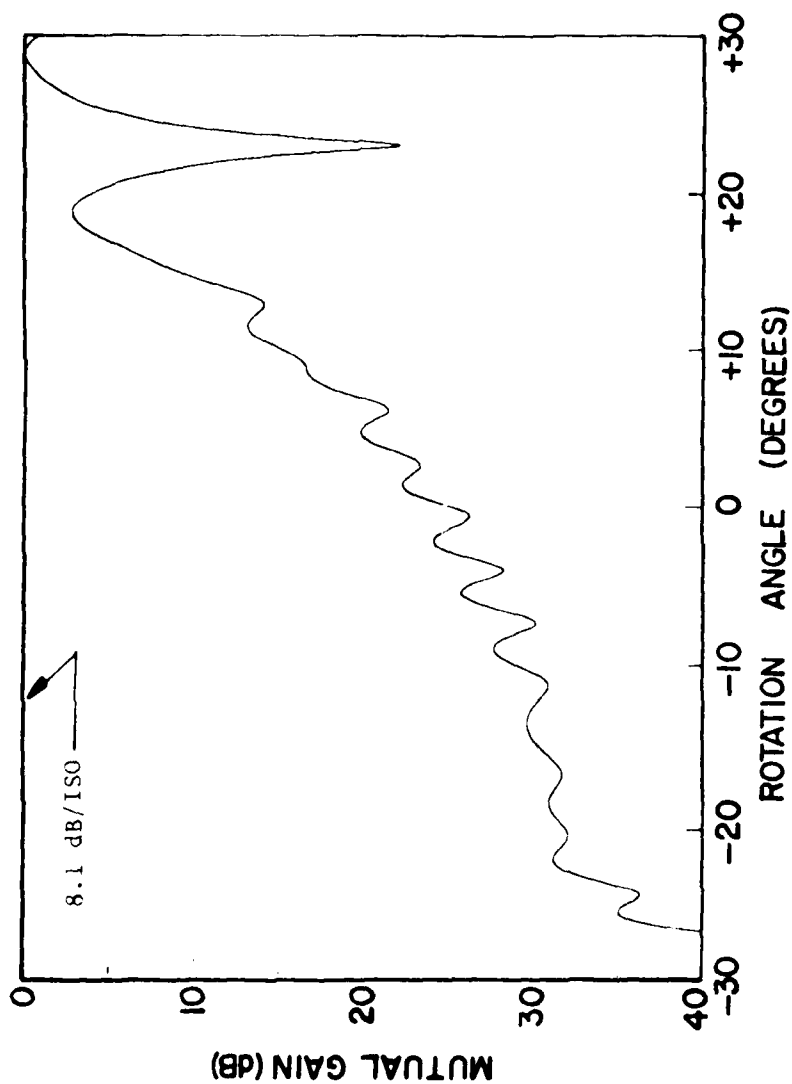


Figure 29. Mutual Gain versus rotation angle for both antennas operating in-band at 5.5 GHz for waveguide feed power flow entirely in the  $TE_{10}$  mode for the longitudinal separation distance  $X = 10$  feet and the transverse separation distance  $Y = 5$  feet.

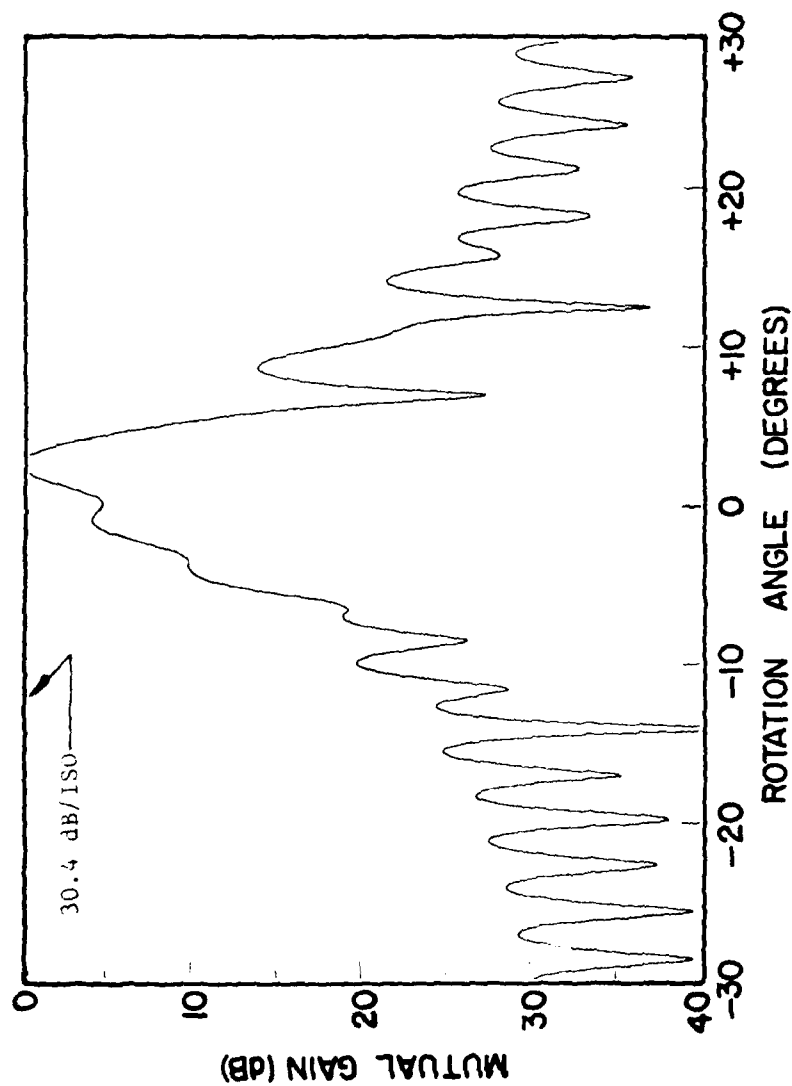


Figure 30. Mutual Gain versus rotation angle for both antennas operating out-of-band at 6.5 GHz for equal waveguide feed power flow in the  $TE_{10}$  and  $TE_{20}$  modes with relative phase angle of 0 degrees for the longitudinal separation distance  $X = 40$  feet and the transverse separation distance  $Y = 0$  feet.



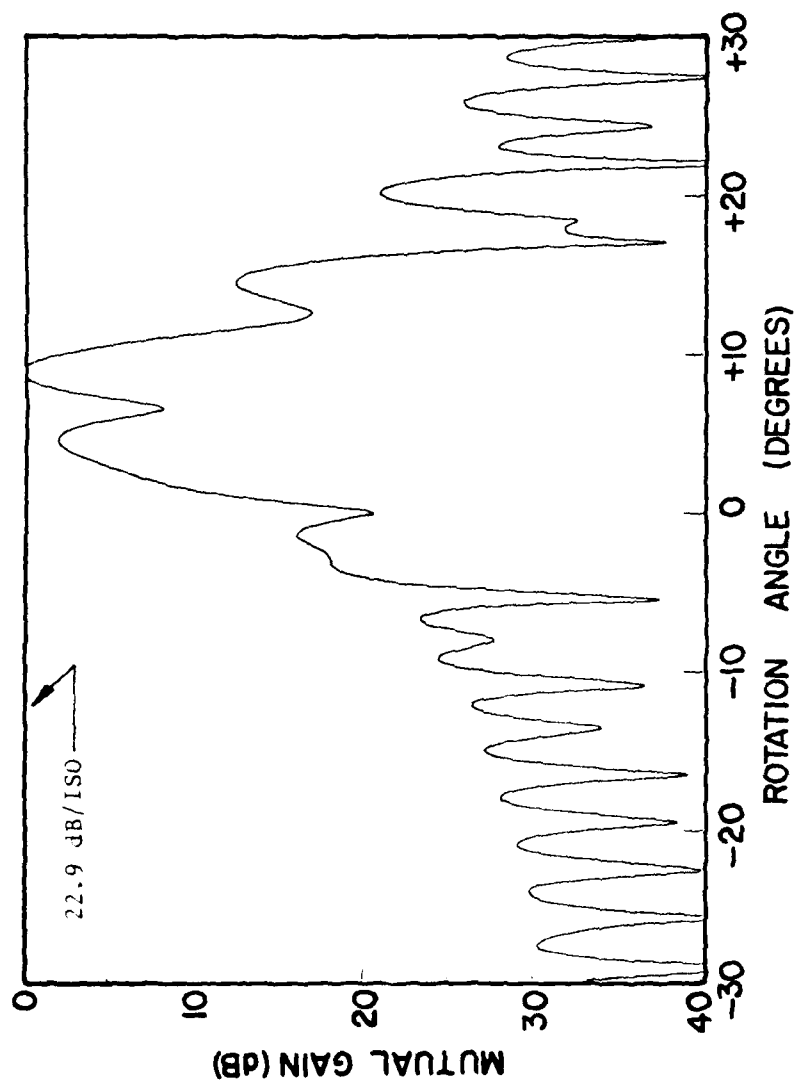


Figure 31. Mutual Gain versus rotation angle for both antennas operating out-of-band at 6.5 GHz for equal waveguide feed power flow in the  $TE_{10}$  and  $TE_{20}$  modes with relative phase angle of 0 degrees for the longitudinal separation distance  $X = 40$  feet and the transverse separation distance  $Y = 5$  feet.

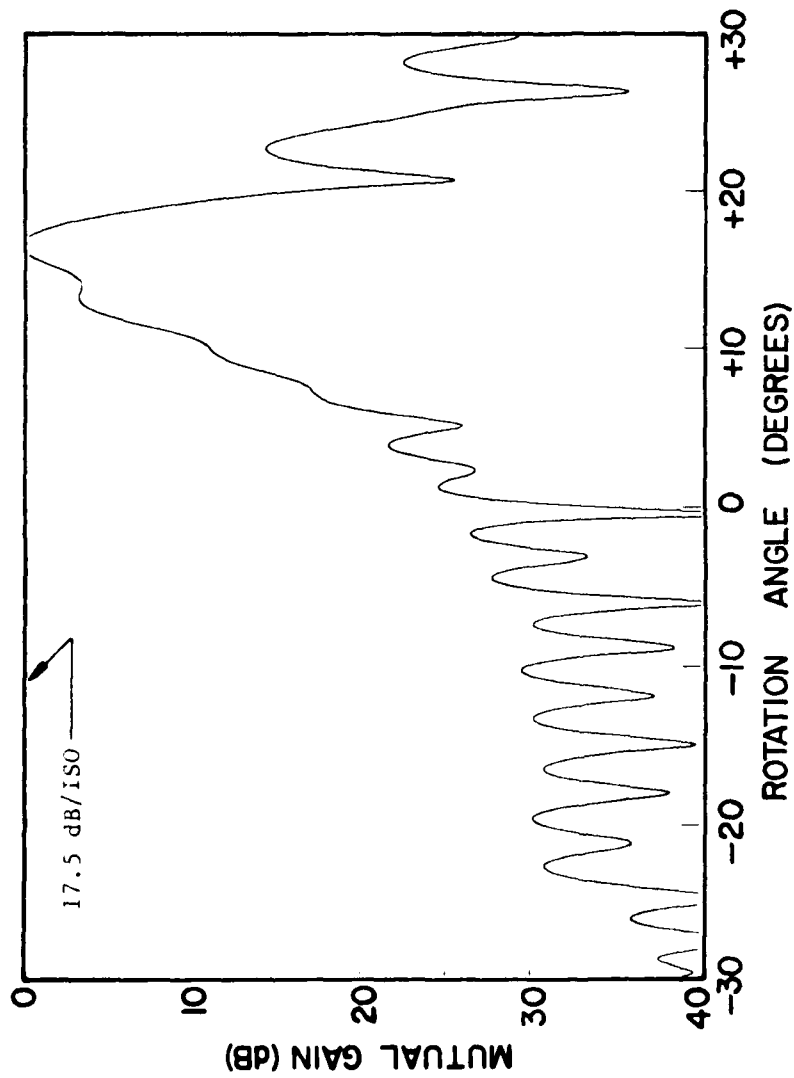


Figure 32. Mutual Gain versus rotation angle for both antennas operating out-of-band at 6.5 GHz for equal waveguide feed power flow in the  $TE_{10}$  and  $TE_{20}$  modes with relative phase angle of 0 degrees for the longitudinal separation distance  $X = 40$  feet and the transverse separation distance  $Y = 10$  feet.

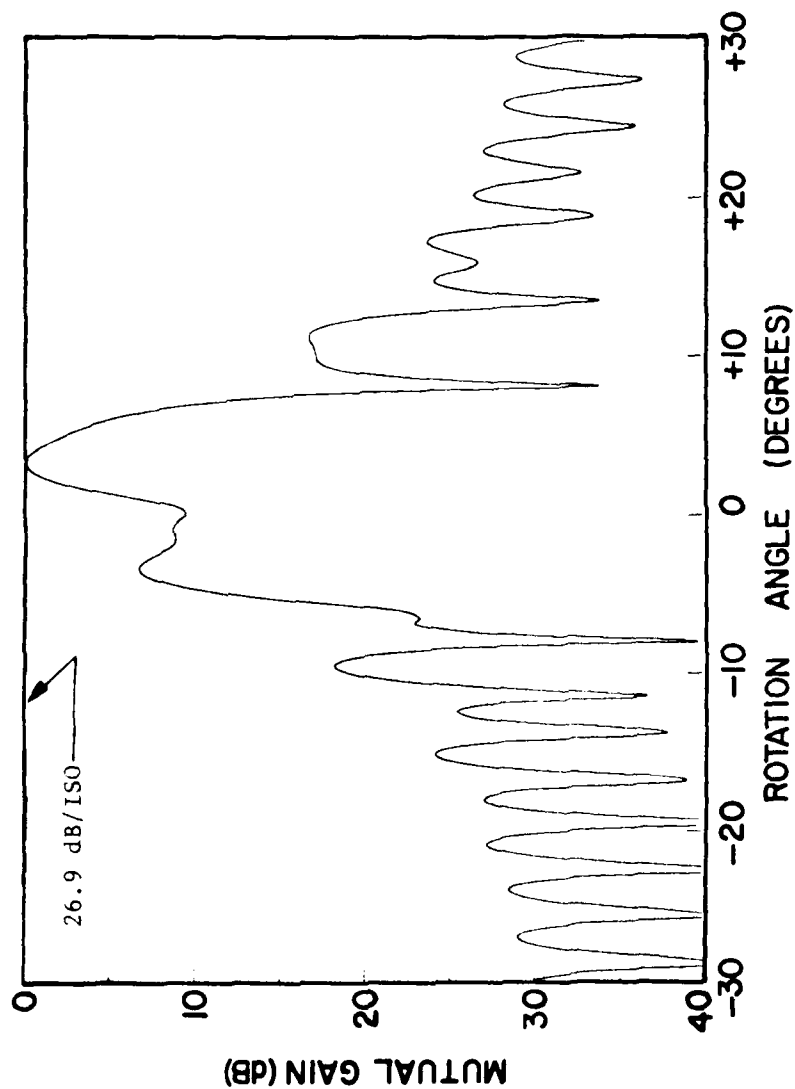


Figure 33. Mutual Gain versus rotation angle for both antennas operating out-of-band at 6.5 GHz for equal waveguide feed power flow in the  $TE_{10}$  and  $TE_{20}$  modes with relative phase angle of 0 degrees for the longitudinal separation distance  $X = 20$  feet and the transverse separation distance  $Y = 0$  feet.

Figure 33.

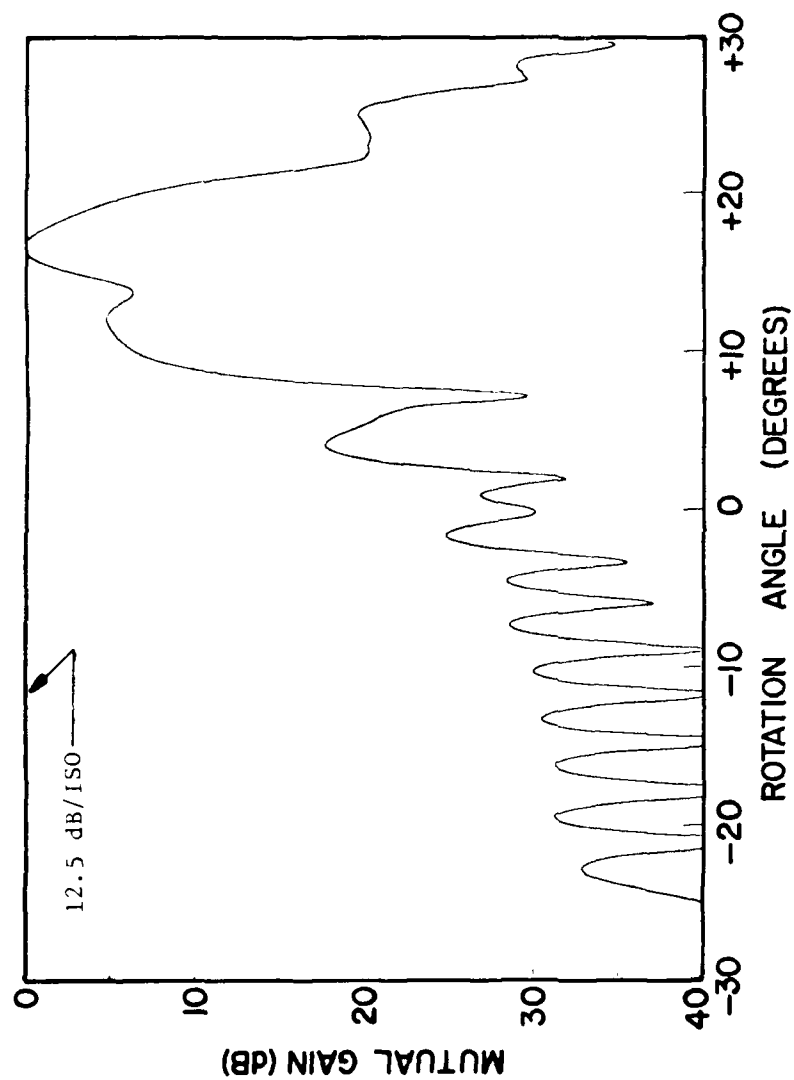


Figure 34. Mutual Gain versus rotation angle for both antennas operating out-of-band at 6.5 GHz for equal waveguide feed power flow in the  $TE_{10}$  and  $TE_{20}$  modes with relative phase angle of 0 degrees for the longitudinal separation distance  $X = 20$  feet and the transverse separation distance  $Y = 5$  feet.

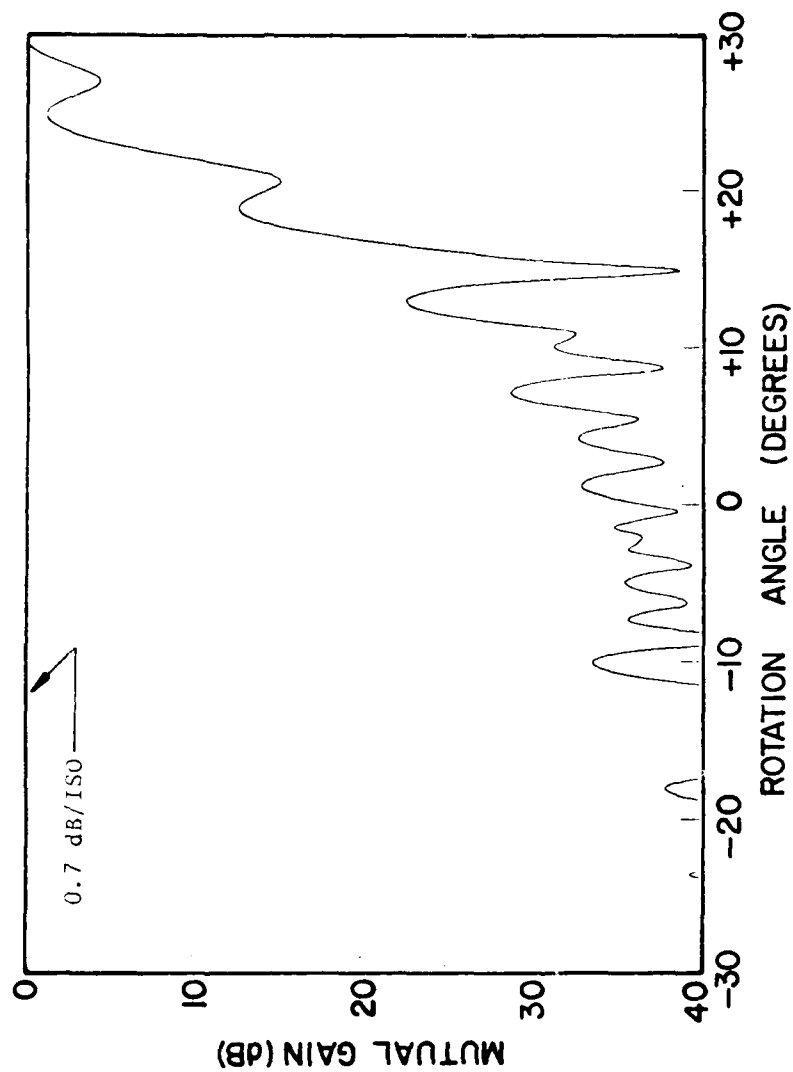


Figure 35. Mutual Gain versus rotation angle for both antennas operating out-of-band at 6.5 GHz for equal waveguide feed power flow in the  $TE_{10}$  and  $TE_{20}$  modes with relative phase angle of 0 degrees for the longitudinal separation distance  $X = 20$  feet and the transverse separation distance  $Y = 10$  feet.

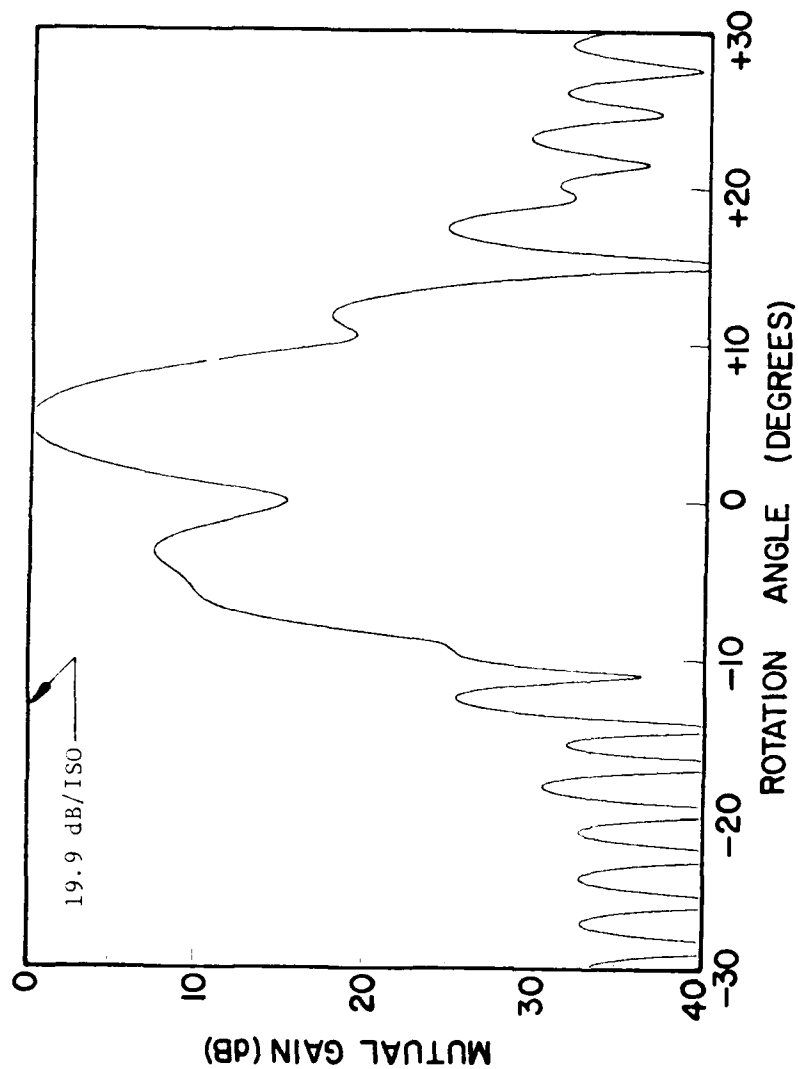


Figure 36. Mutual Gain versus rotation angle for both antennas operating out-of-band at 6.5 GHz for equal waveguide feed power flow in the  $TE_{10}$  and  $TE_{20}$  modes with relative phase angle of 0 degrees for the longitudinal separation distance  $X = 10$  feet and the transverse separation distance  $Y = 0$  feet.

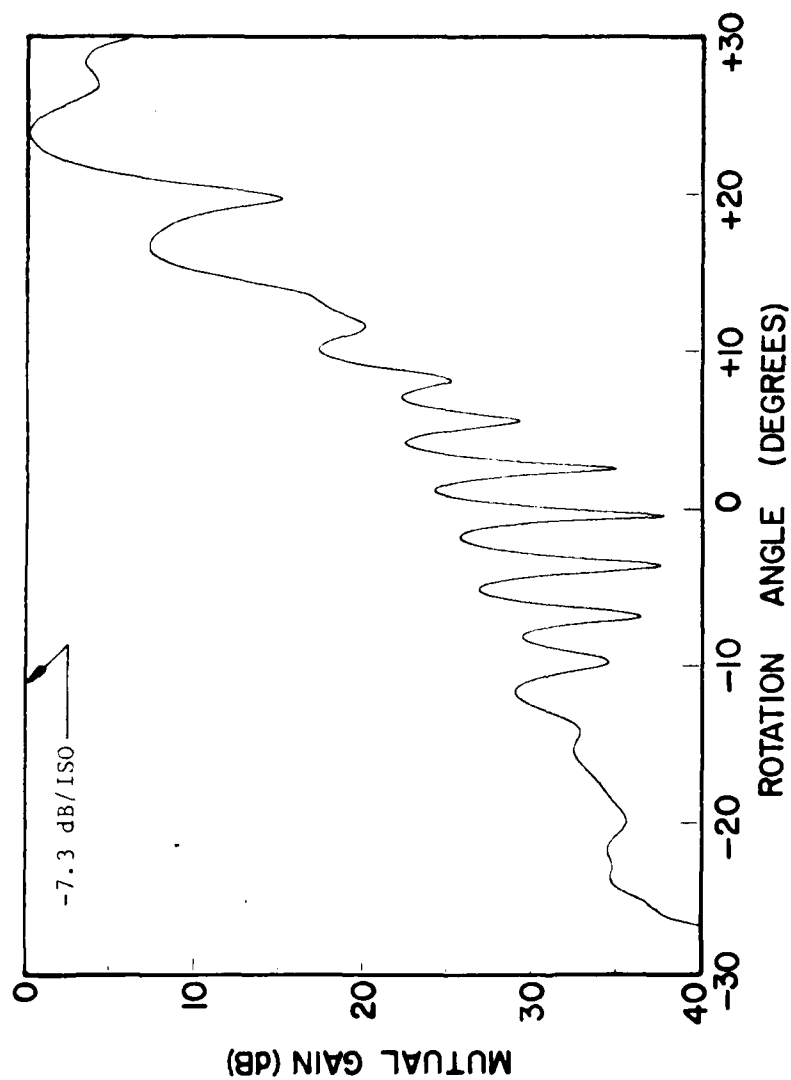


Figure 37. Mutual Gain versus rotation angle for both antennas operating out-of-band at 6.5 GHz for equal waveguide feed power flow in the  $TE_{10}$  and  $TE_{20}$  modes with relative phase angle of 0 degrees for the longitudinal separation distance  $X = 10$  feet and the transverse separation distance  $Y = 5$  feet.

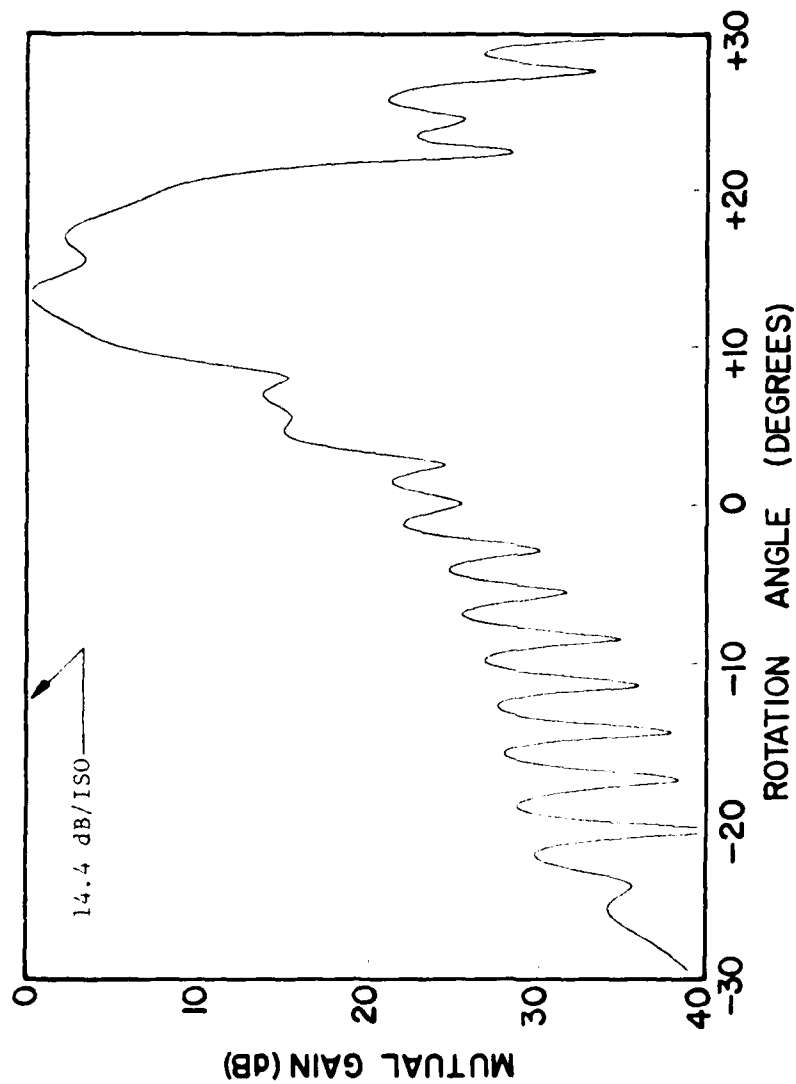


Figure 35. Mutual Gain versus rotation angle for both antennas operating out-of-band at 6.5 GHz for equal waveguide feed power flow in the  $TE_{10}$  and  $TE_{20}$  modes with relative phase of 35 degrees for Antenna A and -50 degrees for Antenna B for the longitudinal separation distance  $X = 20$  feet and the transverse separation distance  $Y = 5$  feet.



plots shown in Figures 22 through 38. First, the peak value of the mutual gain decreases with increasing lateral displacements for a fixed longitudinal displacement. Second, the peak value of the mutual gain increases with increasing longitudinal displacement for a fixed lateral displacement. Both of these trends are consistent with theory. However, the peak mutual gain may exhibit "peaks" and "valleys" if the computation were made for a "finely-grained" set of coordinates. Nevertheless, the "envelope" of the peak mutual gain would exhibit the cited trends.

The peak mutual gain for the in-band to in-band situations always occurs at, or very near to, the rotation angle at which Antenna B points at the center of Antenna A, whereas the peak mutual gain for the out-of-band to out-of-band situations is shifted a few degrees. The direction and magnitude of the angular shift depends on the mode excitation in the feeds of the two antennas as shown by comparing Figure 38 with Figure 34. Also note that the magnitude of the peak mutual gain varies with mode excitations. All of these trends are consistent with theory in the sense of "coarse-grained" behavior mentioned previously.

## SECTION IV

### SUMMARY

The basic theory and equations have been derived (1) to describe the radiation characteristics of a wideband CW or pulsed antenna from measured near-field data and (2) to describe the electromagnetic coupling characteristics of a near-field, cosited pair of wideband CW or pulsed antennas. The theory and equations are applicable for both in-band and out-of-band situations and for stochastic as well as deterministic processes. Numerical simulations have been conducted to validate the analytical results and gain insight into the general behavior of the radiation and coupling characteristics of CW antennas.

The results of the Task 1 investigations conducted to date imply that the fundamental technical requirement for employing near-field techniques for describing stochastic wideband CW or pulsed antenna radiation characteristics is that one be able to compute the statistical average far-field power pattern versus frequency. This requires a knowledge of the near-field covariance functions. The near-field covariance function for a phased array antenna can be estimated with good accuracy if the inter-element coupling is "sufficiently weak". Techniques for determining the covariance function for moderately-coupled or strongly-coupled elements are currently under investigation. Decisions regarding the kinds of additional numerical simulations that are needed in the Task 1 area can best be made after the present covariance investigation is completed. However, it appears that numerical simulations for pulsed and/or two dimensional CW antennas would be beneficial.

The results of the Task 2 investigations conducted to date also imply that the fundamental technical requirement for describing the electromagnetic coupling characteristics of a pair of wideband CW or pulsed cosited antennas is that one be able to compute the average coupling versus frequency. This requires a knowledge of the far-field covariance functions for each antenna. The far-field covariance functions for a reflector antenna fed by a single

waveguide feed can be computed from the covariance functions of the excitation coefficients of the propagating modes in the waveguide feed. The far-field covariance functions for any antenna, phased array or reflector, can always be computed from the near-field covariance functions. Current plans call for numerical simulations for stochastic antenna coupling and for two-dimensional reflector antenna coupling.

## SECTION V

### REFERENCES

1. B.J. Cown and C.E. Ryan, Jr., "Near-Field Theory and Techniques for Wideband Radiating Systems At In-Band and Out-of-Band Frequencies", Georgia Institute of Technology, Interim Technical Report No. 1, Contract No. DAAG29-78-C-0029, January 1979.
2. B. Ye. Kinber, "Decoupling of Closely Situated Reflector Aerials", Radiotekhnika i elektronika, (Russian) Vol. 6, No. 6, pp. 907-916, 1961.
3. Geoffrey Morris, "Coupling Between Closely Spaced Back-to-Back Paraboloidal Antennas", IEEE Trans. on Antennas and Propagation, Vol. AP-28, No. 1, January 1980, pp. 61-64.